Using Linear Stability Analysis as a Tool to Evaluate Jet and Cavity Flow Control Situations

Praveen Panickar* **and Ganesh Raman****
Fluid Dynamics Research Center, Illinois Institute of Technology, Chicago, IL–60616
Raman@iit.edu

ABSTRACT

Flow control has the potential to improve the efficiency of aerospace systems. The design of a flow control system requires knowledge of flow phenomena including information on the evolution of naturally occurring disturbances in the flow. Natural flow disturbances can evolve at various frequencies and growth rates and can assume various mode shapes. Knowledge of the behavior of natural flow instabilities could aid actuator selection and strategy for flow control. In this paper we use linear stability analysis as a tool to analyze jet and cavity flow control situations. We present results from a linear stability study of the resonant acoustic mechanisms in subsonic impinging jets and subsonic cavity flows using the compressible Rayleigh equation. In an impinging jet, the subsonic instabilities are known to be responsible for the acoustic feedback, which is an essential link in setting up the resonances associated with this flow. The instabilities of the helical type are also relevant from the standpoint of the necessity of their existence for jet interactions that may occur in twin nozzle configurations. In the first part of this paper, we focus on helical instability modes in an impinging, high subsonic Mach number jet and examine parameters governing their existence. Using the axisymmetric compressible Rayleigh equation in conjunction with realistic mean velocity profiles, we show that the subsonic helical instabilities in impinging jets are dependent on the jet momentum thickness. Our studies show that at higher subsonic jet Mach numbers, the helical instabilities can exist even at large streamwise locations, indicating that they could play a significant role in the resonance mechanism for a large range of stand-off distances. In the second part of the paper, we use linear stability theory to examine two flow control techniques used in cavity flows. The first control technique acts in a way as to physically lift the shear layer and de-tune the pre-existing resonance feedback loop. The second control technique uses spanwise coherent vortex shedding downstream of a cylindrical rod in order to provide resonance suppression. Linear stability calculations using the two-dimensional compressible Rayleigh equation in conjunction with experimentally measured mean velocity profiles are performed in order to highlight further differences between the two techniques. Experimental measurements of the instability amplitude of the spatially amplified modes in the shear layer show excellent agreement with results predicted using linear stability theory. It is hoped that a knowledge of the physical mechanisms occurring in these feedback enhanced flows could prove essential in designing actuators used to suppress/eliminate the resonances occurring therein.

1. INTRODUCTION

Flow control is more effectively accomplished if one has knowledge of the instability characteristics of naturally occurring disturbances in the flow. Studies of instability characteristics of shear layers present in aerospace applications can aid in designing actuators that can produce excitation signals at frequencies and modes where the flow responds favorably. For example, if flow instabilities in an axisymmetric jet have a natural tendency (under chosen operating conditions) to evolve in a helical mode, control may be more easily accomplished by forcing helical modes. In this example, one would

*Currently at: CRAFT Tech, NCPA, University of Mississippi, University, MS – 38677

**Associate Dean for Research

design actuators located circumferentially around the nozzle exit and vary the relative phase of the actuation signal by $n\theta$ (n is the azimuthal wavenumber and θ is the angular separation of the actuators about the circumference) in the azimuthal direction, while holding the amplitude constant (see Raman *et al*.[1] and Raman and Cain[2]). Similarly, one could use the same actuator array to force the $n = \pm 1$ mode by proper phasing of the actuators. In other situations, multiple frequencies corresponding to naturally occurring fundamental and subharmonic frequencies can be excited (Raman and Rice[3]). In the present work, we use linear stability analysis to examine aerospace flow control situations that involve resonant acoustic flows. Resonant acoustic flows are a special class of fluid flows wherein the acoustics and instabilities in the flow are amplified by a feedback mechanism. As their name suggests, these flows are characterized by an acoustically reverberant environment, which is both set-up and maintained by the aforementioned feedback mechanism; for this reason, such flows are also known as self-sustained flows. There are many instances of resonant acoustic flows that are physically relevant to the aerospace industry. This includes jet screech [4, 5], impinging jets and cavity flows. For the purpose of this paper, we shall restrict ourselves to two examples: namely, subsonic impinging jets and subsonic cavity flows.

1.1. Impinging Jets

When a free jet at a high enough Mach number, typically $M_j \geq 0.65$, impinges on a solid obstacle placed normal to the jet axis, it leads to the production of high amplitude, narrow-band resonant acoustic tones called jet impingement tones. A schematic of the impingement tone generation mechanism is shown in figure 1(a). The solid obstacle, or the wall, in this case is also referred to as the 'ground plane'. The study of impinging jets is relevant to short/vertical take-off and landing (S/VTOL) aircraft such as the Harrier which employ twin axisymmetric nozzles that can rotate in a way as to vector thrust towards the ground to help the aircraft take off. In the case of impinging jets, the physical situation leading to the production of resonant acoustic tones can be explained as follows: the shear layer instabilities produced at the nozzle lip travel downstream and impinge on the ground plane giving rise to acoustic waves. These acoustic waves travel upstream and strengthen the newly produced instabilities at the nozzle lip thereby closing the feedback loop. In the case of impinging jets, the distance of the ground plane from the nozzle exit, known as the stand-off distance, expressed nondimensionally as h/D_j, where D_j is the jet diameter and h is the stand-off distance, is an important parameter in the prediction of the impingement tone frequency.

1.2. Cavity Flows

The cavity flow resonance situation occurs when freestream air flows over an open cavity. Such flow situations occur in a wide variety of practical situations ranging from air flowing over the open sun-roof of a car to more aerospace-specific applications such as flows over open weapons bays and landing gear wells. The resonant acoustic production mechanism for cavity flows is qualitatively similar to that of impinging jets, and can be described as follows: hydrodynamic disturbances in the freestream air flowing over a cavity impinge on its downstream edge, giving rise to acoustic waves. These acoustic waves propagate back upstream and further excite the newly formed disturbances at the upstream edge of the cavity, thereby closing the feedback loop. A schematic of the cavity resonance generation mechanism is shown in figure 1(b). In the case of cavity flows, the distance, L, between the upstream and downstream edges (i.e., the length of the cavity) is one of the length scales of importance. In most studies, this length scale is non-dimensionalized using the depth of the cavity, D, and is called the L/D ratio of the cavity. However some studies also use the L/θ_0 ratio to quantify a cavity, where θ_0 is the momentum boundary layer thickness at the upstream edge of the cavity. The L/θ_0 ratio provides a better understanding of the characteristics of various experimental facilities as it gives an idea of the upstream boundary layer thickness, and by extension, the initial shear layer thickness which plays a role in determining the amplitude of the acoustic and hydrodynamic instabilities.

1.3. Prediction of Acoustic Instability Frequency

In the first part of the paper, we will examine instability modes in high speed impinging jets. In impinging jets, Neuwerth[6] was among the first to predict experimentally observed resonant instability frequencies. Expressing the instability frequency, f, in terms of the Strouhal number, St, the impingement tone resonant frequency is given by:

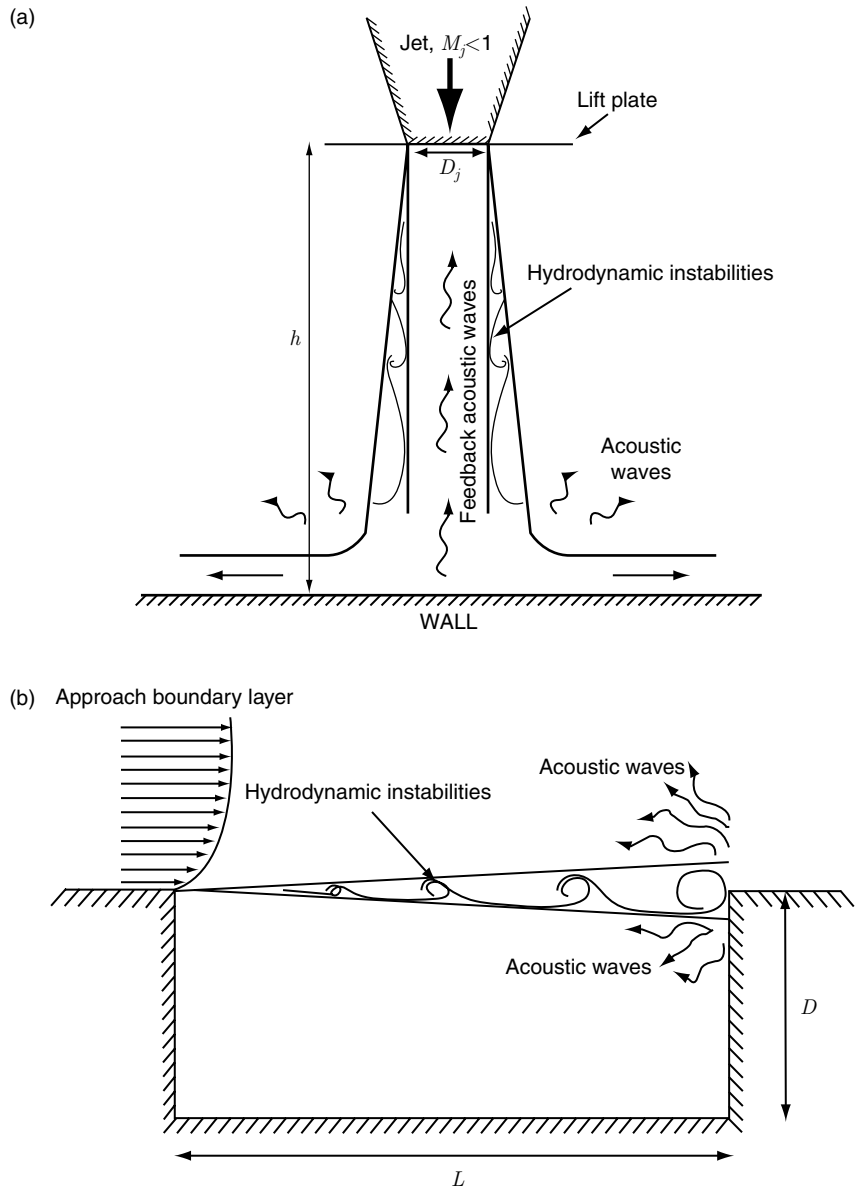

Figure 1. Schematics of the (a). Impinging jet, and (b). Cavity flow resonance generation mechanisms.

$$St = \frac{fD_j}{U_j} = \frac{k\kappa}{h / D_j(1+\kappa M_j)}, \tag{1}$$

where U_j is the jet velocity and κ is the ratio of the jet velocity to the instability convective velocity. The value of κ is generally selected as the one that best fits experimental data to equation (1). In impinging jets, the instability mode staging phenomenon is most prominently seen when the stand-off distance is varied by keeping the Mach number constant.

As far as cavity flows are concerned, although the experimental work of Roshko[7] and the Schlieren visualizations by Krishnamurty[8] preceded him, Rossiter[9] was the first to propose a semi-empirical formula to predict the frequency of the resonant instabilities in cavity flows. Recognizing that the velocity scale associated with the hydrodynamic instabilities is the freestream velocity, u_∞, the Strouhal number is given by:

$$St = \frac{fL}{u_\infty} = \frac{k-\beta}{M+1/\kappa}, \tag{2}$$

where L is the length of the cavity, M is the freestream Mach number and β and κ are empirical constants. Equation (2) is similar to equation (1) when the parameter $\beta = 0$. β represents the phase lag between the passage of a hydrodynamic disturbance downstream past the cavity trailing edge and the formation of a corresponding upstream traveling acoustic disturbance. Similar to κ, the value of β is chosen to best fit the experimental data; Rossiter suggested values of $\kappa = 1/1.75$ and $\beta = 0.25$. Later experiments by Heller, Holmes and Covert[10] on shallow cavities showed that the resonant frequency for cavity flows could be better predicted using a slightly modified form of Rossiter's semi-empirical formula which was expressed as:

$$St = \frac{fL}{u_\infty} = \frac{k - \beta}{M[1 + [(\gamma - 1)/2]\ M^2]^{-1/2} + 1/\kappa}. \tag{3}$$

1.4. Control of Cavity Resonant Tones

In the second part of the paper, we shall examine cavity resonance control techniques using elements from linear stability analysis in an attempt to understand the differences in the stability mechanisms of flows with and without control. In their review paper, Cattafesta *et al.*[11] provided a classification of the various control techniques in use for suppressing cavity resonant tones. This classification scheme was also used in the review paper by Rowley and Williams[12]. As per this classification, cavity resonance control techniques could be divided into two broad categories, namely, passive or active, depending on whether or not the technique used external energy input. The traditional method for controlling cavity resonance is by using devices that are empirically designed, passive in nature - meaning that they cannot adjust to changing operating conditions - and bulky in appearance. These devices operate in a way that eliminates the primary resonance frequencies produced in the cavity. Recently, interest has been aroused in a new technique involving high frequency excitation of the shear layer that has the advantages of simple design geometry and wide operating range of effectiveness. The emergence of this high frequency excitation technique has resulted in a revised resonance control classification scheme. As per this scheme, active flow control (AFC) techniques can be classified as either AFC-I or AFC-II (see Raman *et al.*[13]). Techniques that excite the flow at frequencies close to the most unstable frequency in the flow are classified as AFC-I, and the techniques that excite the flow at frequencies in the Kolmogorov inertial subrange (high frequency excitation) are classified as AFC-II. In the current paper, one of the resonance control techniques studied is a configuration that introduces high frequency excitation into the shear layer over the cavity.

2. OBJECTIVES

The primary objective of the current work is to perform linear stability analysis using the compressible Rayleigh equation in order to obtain physical insights into the resonant acoustics mechanism occurring in subsonic impinging jets and subsonic cavity flows. With this in mind, the specific objectives of this paper are as follows:

1. Understand the stability characteristics of the axisymmetric and helical instability modes in a subsonic impinging jet and justify the presence of helical instabilities in subsonic axisymmetric impinging jets using realistic mean velocity and density profiles.
2. Examine the relationship between the azimuthal instability modes and stand-off distance in axisymmetric impinging jets.
3. Understand the differences in the nature of the flow evolution for cavity resonance control configurations employing shear layer lift-of and high frequency excitation.
4. Study the growth rate of the instability modes in the two-dimensional subsonic flow over a cavity using experimentally measured mean velocity profiles for the baseline and two control configurations.

3. BACKGROUND AND MOTIVATION

3.1. Past Work on Impinging Jets

Much of the early work on subsonic impinging jets can be found in the works of Marsh[14], Wagner[15], and Neuwerth[6]. These papers described the frequency staging phenomena and proposed the formula for predicting the resonant frequency. They revealed that in order to produce stable

impinging tones, the Strouhal number of the instability frequency had to match the Strouhal number of the Kelvin-Helmholtz instability in an axisymmetric free jet. Later, numerical work done on axisymmetric free-jets helped researchers gain additional insight into the instabilities that led to the resonant acoustics mechanism in impinging jets. Morris[16] presented the results of a linear stability analysis study on the spatial viscous instabilities in axisymmetric jets using three representative mean velocity profiles: a top-hat profile (representative of flow close to the nozzle exit), a profile which is representative of the developing jet, and finally, one that describes a jet towards the end of the potential core. More recently, Morris and Bhat[17] studied the spatial evolution of instabilities in elliptic, compressible jets.

With specific focus on subsonic impinging jet flows, Tam and Ahuja[18] provided answers to a number of questions regarding the impinging jet behavior using the vortex-sheet model for compressible inviscid jets. This work was important because it showed, using a Strouhal number mismatch theory, that the impingement tones could not be sustained below a Mach number of 0.65. Using $St = 0.7$ as the cutoff below which the feedback acoustic waves could sustain impingement tones, they showed that at subsonic Mach numbers, portions of the dispersion relation satisfied the cutoff Strouhal number requirement. In addition, they also showed, using the pressure distribution of the eigenfunctions, that the feedback mechanism in subsonic impinging jets occurred from within the jet column. More recently, the authors of the current work re-examined the vortex-sheet model and were able to justify the existence of helical instabilities in subsonic impinging jets (Panickar and Raman[19]). The presence of helical modes in subsonic impinging jets was an important finding since it indicates a possibility of phase-locked interaction between jets when operating in a twin-nozzle configuration (as shown in the work of Seiner, Manning and Ponton[20]). Panickar and Raman[19] also showed that the threshold Mach number for the existence of the helical mode depended on the jet temperature. As the jet temperature increased, the threshold Mach number, above which helical modes could exist, decreased. Additionally, the experimental results revealed that the threshold Mach number also depended on the stand-off distance. In the current paper, we extend the analysis further by incorporating realistic mean velocity and density profiles into our flow model.

3.2. Past Work on Cavity Flows

As far as cavity resonance suppression efforts are concerned, past studies have indicated the effect of high frequency excitation in reducing the energy contained within large scales, especially with increasing streamwise locations (Vlasov and Ginevskiy[21]). However, interest in using high frequency excitation as a possible means of shear flow control was sparked by the work of Wiltse and Glezer[22]. This work reported that exciting the shear layer of a rectangular jet at frequencies that were an order of magnitude lower than the Kolmogorov scales resulted in a redistribution of power in the spectral components. At frequencies below the excitation frequency, the forced flow had lower energy than the unforced flow, while at frequencies greater than the excitation frequency, the forced flow had higher energy than the unforced flow. Simulations of high-frequency excitation of a plane wake performed by Cain *et al.*[23, 24] showed that even though forcing did increase the dissipation rate by as much as 14%, it also reduced the turbulence energy production rate by 24%.

With regard to high frequency excitation for cavity flows, Stanek *et al.*[25] reported dramatic resonance suppression effects using a bank of powered resonance tubes and a cylindrical rod in crossflow arrangement. Here, it must be noted that McGrath and Shaw[26], followed by Shaw[27], were among the first to use a cylindrical rod-in-crossflow configuration as a technique to control cavity resonances. Following the initial round of testing described in Stanek *et al.*[25], a new model was proposed and supporting arguments in its favor were presented in the paper by Stanek *et al.*[28]. According to this model, the dramatic effects of high frequency forcing were an end result of stabilizing the shear layer (i.e. the velocity profile of the flow in the excited configuration was more stable than that in the baseline configuration). Arunajatesan *et al.*[29] used hybrid RANS-LES simulations and concluded that in spite of the large spread caused due to the presence of the cylinder in crossflow configuration, the resonance suppression was brought about due to the fact that the shear layer was lifted up in a way that it did not directly impinge on the aft wall of the cavity. In a more recent study, Ukeiley *et al.*[30] tested and compared the efficacy of two devices - a rectangular fence and a cylinder-in-crossflow - in suppressing fluctuating pressure loads associated with resonant cavity flows. In the current paper we shall examine the differences in the stability characteristics of two cavity resonance control configurations; the first that does not introduce high frequency excitation and the second that introduces high frequency excitation by the use of a cylinder in crossflow setup.

4. EXPERIMENTAL SETUP AND INSTRUMENTATION

All the experiments described in this paper were conducted at the Fluid Dynamics Research Center of the Illinois Institute of Technology. The experiments on the impinging jet were conducted in the Impinging Jet Facility which has been described in detail in the paper by Panickar and Raman[19]. The cavity flow experiments were conducted in the modified High Speed Flow Facility. The reminder of this section will describe the setup and instrumentation of this latter facility.

The freestream air supply is obtained from a reservoir of compressed air which first passes through a plenum before exiting into the ambient through a rectangular slot nozzle having aspect ratio 5. The interior of the nozzle has an elliptical contour in order to ensure smooth flow at the exit. An aluminium block containing the cavity in the form of a rectangular cutout is center mounted flush with the bottom edge of the nozzle. For the experiments presented in this paper, only subsonic freestream Mach numbers were considered. This eliminated added complexities of shocks at the nozzle exit and the interaction between screech tones and cavity resonant tones. It was verified that the area where the cavity was located lay within the potential core of the jet thereby ensuring a uniform freestream flow over the cavity.

The cavity used in the experiments had a length (L) of 25.4 mm and a depth (D) of 12.7 mm giving a length-to-depth ratio of $L/D = 2$. Additionally, the cavity had a width (W) of 25.4 mm. This was the baseline configuration of the cavity. The upstream edge of the cavity was located at a distance of 19.05 mm from the nozzle exit. The boundary layer thickness at the upstream edge of the cavity was measured to be $\delta = 0.80$ mm. Initial experiments on the baseline configuration showed that the resonant frequency at a freestream Mach number $M = 0.60$ was approximately 3200 Hz. One control configuration, referred to as the 'shedding' configuration, consisted of a rod having diameter $d = 0.79$ mm ($D/d = 16$, $\delta/d = 1.00$), supported on either side by rectangular brass posts that had cross section dimensions of 3.18 mm $\times$ 1.59 mm, positioned as close as possible to the leading edge of the cavity. For the current experiments, at $M = 0.60$, the Reynolds number (Re) based on the cylinder diameter, d, and the freestream velocity, u_∞, has been calculated to be $Re_d \sim 9000$. In this range the shedding Strouhal number can be assumed to be constant at $St_s = 0.20$. The shedding frequency for this cylinder diameter, based on the freestream velocity corresponding to $M = 0.60$, assuming $St_s = 0.2$, is approximately 50 kHz, which is more than one order of magnitude greater than the resonant frequency of the baseline cavity. The data presented in this paper for the shedding configuration are for $h = 2.1$ mm (h is the distance between the upstream edge of the cavity and the centerline of the rod in the transverse coordinate dimension), i.e. the rod was located above the boundary layer at the upstream edge of the cavity ($h/\delta = 2.63$), in the freestream flow. Thus, the gap (g) between the upstream edge of the cavity and the bottom of the cylinder for the shedding configurations was $g/\delta = 2.14$ ($h = g + d/2$). The second control configuration was obtained by reducing the gap between the bottom of the cylinder and the upstream edge of the cavity to $g = 0$. Since, in this configuration, there is no mechanism for Kármán vortex street, this will be referred to as the 'nonshedding' configuration. A schematic of the various configurations studied in the current work is shown in figure 2.

For the cavity experiments, acoustic measurements were obtained using a 6.35 mm Brüel & Kjær microphone (model 4939) located on the center of the cavity floor, i.e. at $x = 1$; $y = -1$; and $z = 0$. The microphone stem, preamplifier and cable were located underneath the cavity in such a way that they were shielded from the freestream flow. Unsteady pressure measurements in the shear layer were obtained using a Kulite pressure probe, model type XCS-062-10D having a probe diameter of 1.58 mm. Velocity profiles in the shear layer were obtained using a miniature total pressure probe having a probe diameter of 0.1 mm. In order to calculate the local Mach number of the subsonic flow, the static pressure at each measurement location was assumed to be constant. While this assumption is not strictly true when making measurements immediately downstream of obstructions, where the streamline curvatures may be significant, it is reasonable for the current work. The total pressure probe was positioned in the shear layer using a precision traversing system manufactured by Velmex, Inc. The motion of the traversing system was controlled by a stepper motor in response to computer inputs. The motion controls were integrated into a LabVIEW program and output to the controller via an RS-232 port. The traversing system consisted of two independently controlled axes that could be configured in a way that measurements could be made in all three coordinate directions. The minimum advance of the system was 6.4 microns for either axes which permitted very precise measurements of the shear layer profile. For the experiments on the impinging jets, acoustic data was acquired using three 6.35 mm Brüel & Kjær

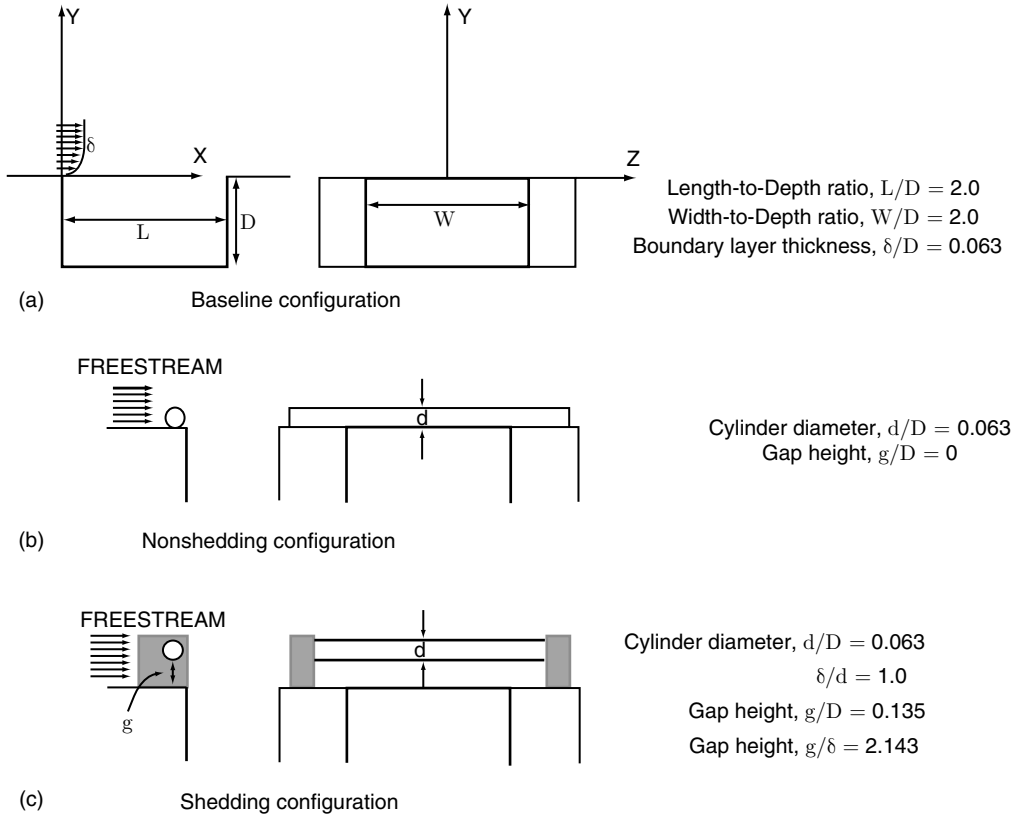

Figure 2. Schematics of the experimental configurations studied in the present work.
(a). Baseline configuration showing coordinate axes setup,
(b). Nonshedding configuration,
(c). Cylinder–in–crossflow configuration that exhibits high frequency vortex shedding (shedding configuration).

microphones located at the jet exit at azimuthal angles of 0°, 90° and 180°. Data for both experiments was acquired using LabVIEW programs and the analog outputs from the transducers and probes were digitized using a National Instruments card.

At this stage it is relevant to discuss the precision, uncertainty and repeatability associated with the experimental scheme. The Impinging Jet Facility and the High Speed Flow Facility are both of the blow-down type and use a bank of four compressors to charge a storage tank that supplies air to their respective plena. The compressors work in a way as to replenish the storage tanks once the air pressure in the tanks falls below a preset value. For the subsonic Mach numbers considered in this paper, taking into account the blow-down nature of the facility, the plenum pressure fluctuated by ± 100 Pa at a given operating condition. The uncertainty in measuring the freestream Mach number associated with this fluctuation was 0.2%. For the spectral measurements, the resonant frequency was extremely repeatable and varied by less than 0.2%. It was found that the SPL levels were the quantities that showed the largest fluctuations in repeatability values, although by careful experimentation, even these variations could be kept down to ± 3 dB.

5. LINEAR STABILITY THEORY AND THE RAYLEIGH EQUATION

Linear stability analyses are traditionally applied to laminar and near-transition flows. That being said, it is well established that even in turbulent flows, the large scale structures are the dominant sources of sound. Since the characteristics of these large scale structures in a high speed flow can be well predicted by a locally parallel, inviscid linear stability analysis, it follows that such an analysis would also be applicable to turbulent free shear flows (Gaster, Kit and Wygnanski[31]). The stability of compressible, inviscid shear layers has been studied extensively in literature (see, for instance, Lees and Reshotko[32] or Michalke[33, 34]). However, for the sake of completeness, the most important equations will be

presented in this section. The interested reader is referred to Rowley[35], or to the review paper by Michalke[36] for a detailed discussion on the linear stability theory of compressible, inviscid shear flows. In the current paper, the focus of interest lies in obtaining the spatial growth rate of the instability mode at a particular Mach number for a given mean velocity distribution.

The traditional starting point for obtaining results using linear stability is to model the flow as a uniform stream bound by a vortex sheet. This model is called the 'vortex-sheet' model. The vortex-sheet model allows us to separate the flow regime into two sharply demarcated regions, each having uniform flow properties. Such an approach greatly simplifies the governing equations which can then, typically, be solved separately for each regime, using analytical expressions. Following this, the two separate solutions are reconciled by requiring these solutions to be continuous across the demarcation boundary. One of the main advantages of using the vortex-sheet model is that it provides analytical expressions for the dispersion relation (the relation between the instability frequency and wavenumber). Additionally, the vortex-sheet model provides reliable estimates regarding the phase velocity of the instabilities. However, in order to reliably estimate the growth rate of these instabilities, one needs to use a more realistic model of the flow. Such a model is commonly referred to as the 'mixing length' model and in the case of compressible, inviscid, parallel flows, this model is represented by the Rayleigh equation. In this section we shall present a brief introduction to the Rayleigh equation in axisymmetric and cartesian coordinates. The former is relevant when studying the stability characteristics of an axisymmetric jet whereas the latter is applicable to flow over a two-dimensional cavity.

For an axisymmetric, compressible and inviscid jet, assuming a locally parallel, isentropic flow, we start out by writing the equations of motion for the flow in cylindrical coordinates. The continuity equation is given by:

$$\frac{\partial \rho}{\partial t}+\frac{1}{r}\frac{\partial}{\partial r}(\rho r v)+\frac{1}{r}\frac{\partial}{\partial \theta}(\rho w)+\frac{\partial}{\partial x}(\rho u)=0, \tag{4}$$

where $\mathbf{u} \equiv (u,\ v,\ w)$ are the velocity components in the axial, radial and azimuthal directions $(x,\ r,\ \theta)$ respectively and ρ is the fluid density. The momentum equations in the axial, radial, and azimuthal directions are:

$$\rho\left[\frac{\partial u}{\partial t}+v\frac{\partial u}{\partial r}+\frac{w}{r}\frac{\partial u}{\partial \theta}+u\frac{\partial u}{\partial x}\right]+\frac{\partial p}{\partial x}=0, \tag{5}$$

$$\rho\left[\frac{\partial v}{\partial t}+v\frac{\partial u}{\partial r}+\frac{w}{r}\frac{\partial v}{\partial \theta}-\frac{w^2}{r}+u\frac{\partial u}{\partial x}\right]+\frac{\partial p}{\partial r}=0, \tag{6}$$

$$\rho\left[\frac{\partial w}{\partial t}+v\frac{\partial w}{\partial r}+\frac{w}{r}\frac{\partial w}{\partial \theta}+\frac{vw}{r}+u\frac{\partial w}{\partial x}\right]+\frac{1}{r}\frac{\partial p}{\partial \theta}=0, \tag{7}$$

respectively, where p is the pressure. Finally, the energy equation, assuming that the fluid is an ideal gas with constant specific heats in the absence of heat addition and body forces, is given by:

$$\frac{\partial p}{\partial t}+v\frac{\partial p}{\partial r}+\frac{w}{r}\frac{\partial p}{\partial \theta}+u\frac{\partial p}{\partial x}+\gamma p\left[\frac{1}{r}\frac{\partial}{\partial r}(vr)+\frac{1}{r}\frac{\partial w}{\partial \theta}+\frac{\partial u}{\partial x}\right]=0, \tag{8}$$

where γ is the isentropic exponent. Note that equations (4)-(8) are nondimensional; the density, ρ is nondimensionalized by the jet centerline density at the nozzle exit, ρ_j, the velocity components are nondimensionalized by the jet centerline velocity at the nozzle exit, U_j, and the pressure is nondimensionalized by the term $\rho_j U_j^2$. The length scale for the problem is selected to be the jet radius,

R_j, although some references ([36]) use the momentum thickness, θ, as the length scale for nondimensionalization.

Under the locally parallel assumption, we decompose the fluid properties into a mean part and a fluctuating part as follows:

$$u(x,r,\theta,t) = \overline{u}(r) + \tilde{u}(x,r,\theta,t), \tag{9}$$

$$v(x,r,\theta,t) = \tilde{v}(x,r,\theta,t), \tag{10}$$

$$w(x,r,\theta,t) = \tilde{w}(x,r,\theta,t), \tag{11}$$

$$p(x,r,\theta,t) = \overline{p} + \tilde{p}(x,r,\theta,t), \tag{12}$$

$$\rho(x,r,\theta,t) = \overline{\rho}(r) + \tilde{\rho}(x,r,\theta,t). \tag{13}$$

In the above equations, note that the mean pressure, $\overline{p}$, is independent of coordinate dimension, indicative of a uniform pressure distribution in the ambient. Substituting the decomposition given in equations (9)-(13) into equations (4)-(8), and neglecting products of fluctuations we get the linearized equations of motion for the flow. Additionally, we can make the simplification:

$$\gamma\overline{p} = \gamma\frac{p_j}{p_j U_j^2} = \frac{a_j^2}{U_j^2} = \frac{1}{M_j^2}, \tag{14}$$

where M_j is the Mach number of the jet.

Next, we decompose the perturbation terms into normal modes given by:

$$[\tilde{u},\tilde{v},\tilde{w},\tilde{p}] = [\hat{u}(r),\hat{v}(r),\hat{w}(r),\hat{p}(r)]e^{i(\alpha x+n\theta-\omega t)}, \tag{15}$$

where, α is the axial wavenumber and n is the azimuthal wavenumber of the instability. The azimuthal wavenumber, n, can take on integral values corresponding to the instability mode of interest (for instance, $n = 0$ corresponds to the axisymmetric mode, $n = 1$ corresponds to the helical mode, and so on). ω is the circular frequency of the instability, and is related to the instability frequency, f, by $\omega = 2\pi f$. $\hat{u},\hat{v},\hat{w}$ and $\hat{p}$ are the eigenfunctions of the velocity and pressure fluctuations corresponding to the normal mode decomposition. Generally speaking, $\omega, \alpha \in \mathbb{C}$, where $\mathbb{C}$ is the set of complex numbers.

Substituting the normal mode ansatz given in equation (15) into the linearized equations of motion and solving for the pressure eigenfunction $\hat{p}(r)$ yields the ordinary differential equation given as:

$$\frac{d^2\hat{p}}{dr^2} + \left[\frac{1}{r} - \frac{1}{\overline{\rho}}\frac{d\overline{\rho}}{dr} + \frac{2\alpha}{\omega-\alpha\overline{u}}\frac{d\overline{u}}{dr}\right]\frac{d\hat{p}}{dr} + \left[\overline{\rho}M_j^2(\omega-\alpha\overline{u})^2 - \frac{n^2}{r^2} - \alpha^2\right]\hat{p} = 0. \tag{16}$$

Equation (16) is a form of the Rayleigh equation for inviscid, compressible, and axisymmetric shear layers. It is the governing equation for the mixing-length model as shown in the work of Michalke[36] and Tam and Ahuja[37].

Following a similar procedure for inviscid, compressible, and two-dimensional shear layer, and using a normal mode decomposition of the form:

$$[\tilde{u}, \tilde{v}, \tilde{p}] = [\hat{u}(y), \hat{v}(y), \hat{p}(y)]e^{i(\alpha x + \omega t)}, \tag{17}$$

the cartesian equivalent of the Rayleigh equation is given by:

$$\frac{d^2\hat{p}}{dy^2} - \left\{\frac{2\alpha}{\omega + \alpha\overline{u}}\frac{d\overline{u}}{dy} + \frac{1}{\overline{\rho}}\frac{d\overline{\rho}}{dy}\right\}\frac{d\hat{p}}{dy} - \left\{\alpha^2 - M^2\overline{\rho}(\omega + \alpha\overline{u})^2\right\}\hat{p} = 0. \tag{18}$$

The two-dimensional Rayleigh equation has been nondimensionalized as follows: the density ρ and the velocity $\mathbf{u} = (u,\ v)$ have been nondimensionalized using the freestream density and the freestream velocity, ρ_∞ and U_∞, respectively, the pressure has been nondimensionalized using $\rho_\infty U_\infty^2$, and the lengths are nondimensionalized using the cavity depth D.

Equations (16) and (18) are solved as differential eigenvalue problems. For spatially developing flows, such as the ones being studied in the current work, a spatial linear stability analysis is relevant. For the spatial stability eigenvalue problem, given the normal mode decompositions in equations (15) and (17), we assume $\omega \in \mathbb{R}$ and look for $\alpha \in \mathbb{C}$ such that Im $(\alpha) = \alpha_i < 0$. In such a situation, the solution is such that it oscillates sinusoidally in time, but grows exponentially in space, corresponding to a *spatial* instability. The differential problem is solved using the shooting method, which is a generalized iterative procedure that is used to solve boundary-value problems, but can be easily modified to solve eigenvalue problems.

5.1. Boundary Conditions

In order to set boundary conditions for the axisymmetric mixing-length model equation (16), it is necessary to examine the behavior of this equation in the asymptotic limit as $r \to 0$ and as $r \to \infty$. The general requirement is that the solution be finite as $r \to 0$ and bounded as $r \to \infty$. With these requirements, the mixing-length model equation is transformed at each boundary as follows:

1. At the right boundary, as $r \to 0$, $\overline{u} = \overline{\rho} = 1$ and $\overline{u}' = \overline{\rho}' = 0$ where primes denote differentiation with respect to the radial coordinate, *r*. This reduces equation (16) to:

$$\frac{d^2\hat{p}}{dr^2} + \frac{1}{r}\frac{d\hat{p}}{dr} + \left[M_j^2(\omega - \alpha)^2 - \alpha^2 - \frac{n^2}{r^2}\right]\hat{p} = 0. \tag{19}$$

The general solution to this equation that is finite at $r \to 0$ is given by:

$$\hat{p}(r = 0) = AJ_n\left[\left(\sqrt{M_j^2(\omega - \alpha)^2 - \alpha^2}\right)r\right], \tag{20}$$

where J_n is the Bessel function of order n.

2. At the left boundary, as $r \to \infty$ and $\overline{u} = 0$, $\overline{\rho} = T_j/T_\infty$ and $\overline{u}' = \overline{\rho}' = 0$. This reduces equation (16) to:

$$\frac{d^2\hat{p}}{dr^2} + \frac{1}{r}\frac{d\hat{p}}{dr} + \left[\frac{\omega^2 M_j^2 a_j^2}{a_\infty^2} - \alpha^2 - \frac{n^2}{r^2}\right]\hat{p} = 0. \tag{21}$$

Since we are looking for wavelike solutions, it is appropriate to express the solution at large distances as Hankel functions rather than regular Bessel or modified Bessel functions. In this case, the general solution to this equation that is bounded as $r \to \infty$ is given by:

$$\hat{p}(r \to \infty) = BH_n^{(1)}\left[\left(\sqrt{\frac{\omega^2 M_j^2}{\beta^2} - \alpha^2}\right)r\right]. \tag{22}$$

In (22), we have made the simplification: $a_\infty/a_j = \beta$, and $H_n^{(1)}$ is the Hankel function of first kind. The constants *A* and *B*, used in equations (20) and (22) respectively, are arbitrary.

For the two-dimensional Rayleigh equation given in equation (18), given the coordinate axes setup shown in figure 2, and the nondimensionalizing length scale, the region of integration extends from $y = -1$ to $y \to \infty$. Bearing this in mind, the boundary conditions are given by:

1. At $y = -1$, we impose the wall boundary condition given by:

$$\frac{d\hat{p}}{dy}(y = -1) = 0, \tag{23}$$

2. The boundary condition at $y \to \infty$ requires the pressure $\hat{p}$ to be bounded at this distance. Since at $y \to \infty$, $\bar{u} = \bar{\rho} = 1$, equation (18) breaks down into a simple, constant coefficient second order differential equation. The solution to this equation that is bounded at ∞ is:

$$\hat{p}(y \to \infty) = Ae^{-\lambda y}, \tag{24}$$

where $\lambda = \sqrt{\alpha^2 - M^2(\omega + \alpha)^2}$.

5.2. Mean Velocity and Density Profiles

In equations (16) and (18), in addition to terms that originate from the normal mode decomposition, there are two additional terms that are, at this stage, unknown, namely the mean velocity and density terms $\bar{u}$ and $\bar{\rho}$ respectively. Since, depending on the coordinate axes setup, both these terms are functions of only the radial coordinate r or the transverse coordinate y, we need to define velocity and density profiles in these directions. The velocity profile is usually selected to match experimentally observed profiles and contain adjustable parameters that reflect the changing nature of the profile as one moves along the streamwise direction. For instance, in the case of the axisymmetric jet, close to the nozzle exit, the velocity profile would be a top-hat, or plug profile; as we move downstream, this top hat profile changes to a reflect a potential core surrounded by a mixing layer and far enough downstream, where the potential core no longer exists, the profile changes to that of a fully-developed jet.

In the current work, we shall use a hyperbolic tangent type of velocity profile given as:

$$\bar{u} = \frac{1}{2}\left[1 + \tanh\left\{a\left(\frac{1}{r} - r\right)\right\}\right]. \tag{25}$$

In the above equation, the parameter a is freely adjustable, and decides the relative streamwise location of the velocity profile. This profile was extensively used in the review paper[36].

In his work, Michalke[36] used the momentum thickness, θ, as the length parameter of choice as opposed to the jet radius, R_j, that is used in the current paper. The free parameter, a, in equation (25) is related to the momentum thickness by the relation:

$$a = \frac{1}{4\theta}. \tag{26}$$

In equation (26), θ has been nondimensionalized using the jet radius, R_j, in order to be consistent with our theory. The momentum thickness for an incompressible jet flow is defined as:

$$\theta = \int_0^\infty \bar{u}\ (1 - \bar{u})\ d \tag{27}$$

Thus, θ is a free parameter that influences the stability characteristics of a perfectly expanded jet. Note that, when used in this context, θ is different from the azimuthal cylindrical coordinate direction. In an actual jet, θ increases as we travel downstream along the jet. This means that θ can be used to characterize the velocity profiles at various axial locations in the jet; a small value of θ indicates a location close to the nozzle exit and a larger value of θ indicates axial locations further downstream along the axial direction. In the case of compressible jet flows, the momentum thickness is defined as:

$$\theta_c = \int_0^\infty \overline{\rho}\,\overline{u}\ (1-\overline{u})\ dr. \tag{28}$$

Thus, the momentum thickness in case of compressible jet flows depends on the density as well as velocity profiles. As will be shown in equation (30), the density profile, and consequently, the compressible momentum boundary layer thickness, θ_c, for a given velocity profile in a compressible jet flow, depend additionally on the Mach number, M_j, and the jet temperature ratio, T_j/T_∞. The influence of these two parameters is not uniform at all operating conditions. For this reason, θ rather than θ_c is selected as the length-scale of choice. Figure 3 shows some sample mean velocity and density profiles illustrating the effect of changing of momentum thickness.

In the work of Crighton and Gaster[38], the following relation was used to correlate the axial position to the momentum thickness:

$$\theta = 0.03x + 0.04. \tag{29}$$

In general, however, this relation is dependent on the nozzle exit conditions and may be different for different jets.

The mean density profile for compressible jet flows can be expressed in terms of the Crocco-Busemann relation and is given (in nondimensional form) as:

$$\overline{\rho} = \left[\frac{1}{2}(\gamma-1)\ \overline{u}\ (1-\overline{u})\ M_j^2 + \overline{u} + \frac{T_\infty}{T_j}\ (1-\overline{u})\right]^{-1}. \tag{30}$$

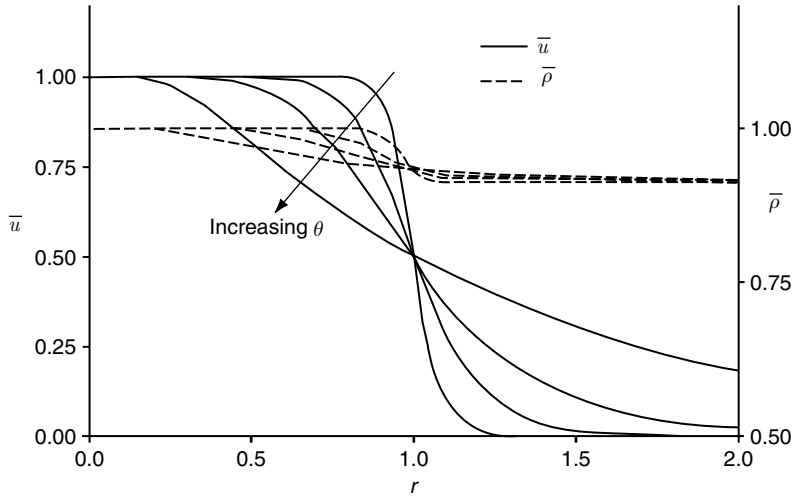

Figure 3. Sample mean velocity profiles for a developing jet.

For the two-dimensional Rayleigh equation, the mean velocity profile is, once again, described by a hyperbolic tangent type relation given as:

$$\overline{u}(y) = \frac{1}{2}\left[1 + \tanh\left\{\frac{2(y + SL_{off})}{\delta_w}\right\}\right], \tag{31}$$

where δ_w is the vorticity thickness of the shear layer and the term SL_{off} accounts for the transverse offset (if present) of the shear layer. It was observed that the velocity profile for the shedding configuration does not agree with the profile equation given in (31). This is because the presence of the cylinder leads to a velocity defect (wake-type velocity profile) in the profiles downstream of the cylinder. For this control configuration the mean velocity profile is a hybrid of the traditional shear layer velocity profile given in equation (31) and a wake profile, and is given by:

$$\overline{u}(y) = \frac{1}{2}\left[1 + \tanh\left\{\frac{2(y + SL_{off})}{\delta_w}\right\}\right] - W_{amp}\,exp\left[-\left\{\frac{y + W_{off}}{W_{wid}}\right\}^2\right]. \tag{32}$$

where W_{amp}, W_{off} and W_{wid} represent the wake amplitude, the wake offset and the wake width respectively. The profile given in equation (32) will be referred to as the hybrid profile. A similar profile was used in the work of Koochesfahani and Frieler[39].

As far as mean density profiles are concerned, one can resort to a two-dimensional version of the Crocco-Busemann equation (equation (30)) used for the axisymmetric Rayleigh equation. However, for low subsonic freestream velocities ($M < 0.8$ studied in [40]), a uniform density assumption also yields satisfactory results. Hence, for the current work where $M = 0.60$, we shall assume

$$\overline{\rho} = 1, \tag{33}$$

for the two-dimensional Rayleigh equation.

When integrating equations (16) and (18), as well as in equations (27) and (28), the upper limit of integration, '∞' is taken to be some large value where the mean profiles are constant.

6. RESULTS AND DISCUSSION

In this section we attempt to gain further insight into the resonant acoustics mechanism in subsonic impinging jets and subsonic cavity flows using elements from linear stability analysis by application of suitable variants of the compressible Rayleigh equation. The work on impinging jets is an extension of the previous work conducted by the same authors ([19]) where the vortex-sheet model was used to justify the presence of helical instability modes seen in the experimental data. Figures 4(a,b) show the variation of the frequency of the dominant instability as a function of the stand-off distance h/D_j at $M_j = 0.90$ and 0.95 respectively. Sample spectra at these two jet Mach numbers are shown in 4(c,d). These figures indicate that, in the time-averaged sense, the helical and axisymmetric modes can not only co-exist at certain stand-off distances, but also that the helical mode can be dominant over the axisymmetric mode at some stand-off distances. At large stand-off distances experimental data did not show the presence of the helical mode at any subsonic Mach number. The mean Strouhal numbers, St_m, for the helical instabilities were greater than those for the axisymmetric modes indicating that the resonant frequencies of the helical instabilities were higher than those of the axisymmetric instabilities. Our linear stability analysis on the basis of the vortex-sheet model showed that for cold jets at Mach numbers $M_j > 0.89$, the dispersion relation for the helical modes lay within the theoretical cutoff limit of Strouhal number ($St < 0.7$) as described in §3.1. This indicates that these modes are permissible, in agreement with our experimental results. In the current work, we shall use the axisymmetric Rayleigh equation with realistic mean velocity and density profiles to understand the relation between the helical modes and the stand-off distance in an attempt to reconcile our experimental observation of helical modes at small stand-off distances.

For the cavity flow experiments, the spectral characteristics of the shedding and nonshedding configurations are shown in figure 5. The spectra reveals that although the broadband levels measured in the baseline configuration are reduced by the order of 2-5 dB depending on the frequency, they are greater than the levels of the shedding configuration. More importantly, the spectra from the nonshedding configuration shows narrowband tonal content at significant amplitudes at frequencies higher than those of the tonal component in the baseline configuration. These higher tonal frequencies show good agreement with the theoretical second Rossiter mode, whereas the dominant frequency in the baseline configuration agrees with the first Rossiter mode. For linear stability calculations using the two-dimensional Rayleigh equation, we measure the mean velocity profiles of the baseline and the two control configurations, shedding and nonshedding, at a location close to the upstream edge of the cavity and compare the growth rates of the instabilities present in these configurations. We also discuss the differences in the evolution of the mean velocity profile along the centerline of the cavity for the two control configurations in order to understand the differences in the physics of the resonance suppression for the two control configurations.

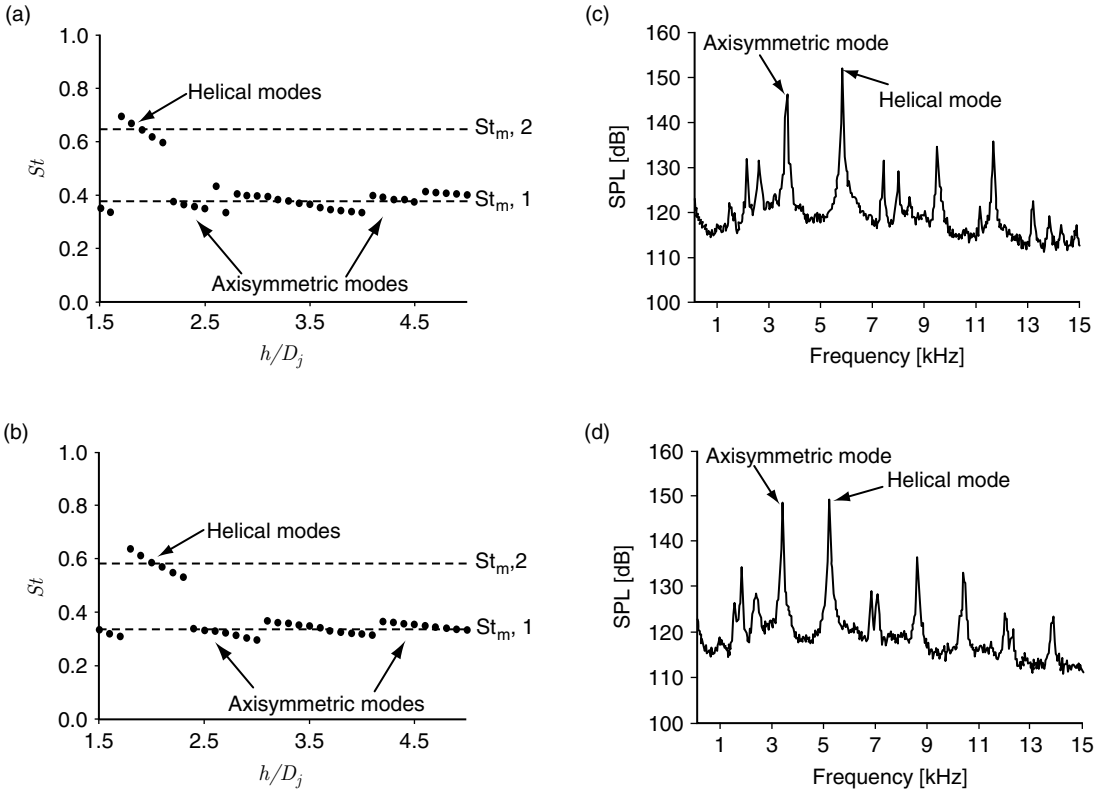

Figure 4. Characteristics of the impinging jet. Instability Strouhal number as a function of the stand-off distance at (a). $M = 0.90$, and (b). $M = 0.95$. Sample spectra showing the co-existence of the helical and axisymmetric instabilities at (c). $M_j = 0.90$, $h/D_j = 2.0$, and (d). $M_j = 0.95$, $h/D_j = 2.3$.

6.1. Impinging Jets and the Axisymmetric Rayleigh Equation

In their work on the three families of instabilities in compressible jets, Tam and Hu[37] showed that in addition to the Kelvin-Helmholtz instability mode, the jet column could sustain two additional modes, namely, the subsonic and supersonic modes. In the context of the vortex-sheet model, the subsonic modes were manifested as neutral solutions whereas the supersonic modes were unstable. Following this work, it was shown in Tam and Ahuja[18] that in the case of impinging jets the feedback acoustic waves that were responsible for closing the resonant feedback loop were the neutral acoustic solutions (or subsonic modes) of the vortex-sheet model. At subsonic jet Mach numbers, these subsonic instabilities have near-zero growth rate even when viewed in the context of the mixing-length model and the axisymmetric compressible Rayleigh equation. In this subsection, we shall examine the variations in the dispersion relation when using the mixing-length model for various momentum thicknesses, θ, at $M_j = 0.90$ and 0.95. We shall also correlate the Mach number of the jet and the momentum thickness tothe existence of the helical instabilities. Since the momentum thickness of the jet is a function of the streamwise position, such a correlation will provide information regarding the stand-off distance at the given Mach number where one can expect the helical mode to exist. For these results it is important to remember that a large value of θ indicates a distance further downstream compared to a smaller value of θ; $\theta = 0$ is equivalent to the vortex-sheet model. Additionally, all the results presented are for the first radial instability mode in cold jets.

We start by examining the dispersion relation for the axisymmetric mode at $M_j = 0.90$. For various momentum thicknesses, these dispersion relation curves are shown in figure 6, where α_r represents the real part, i.e. $\mathrm{Re}(\alpha)$, of the eigenvalue. As shown in this figure, the dispersion relation for the axisymmetric mode lies within the permissible range of Strouhal numbers for all the momentum thickness values over a large range of α values. To put this in perspective, a momentum thickness value of $\theta = 0.5$ corresponds to a velocity profile indicative of regions towards the end of the potential core. For strong impingement tones, the stand-off distance should ideally be located within the potential core of the jet. Since the dispersion relation for the axisymmetric mode at $M_j = 0.90$ lies within the permissible range of Strouhal number, figure 6 indicates that

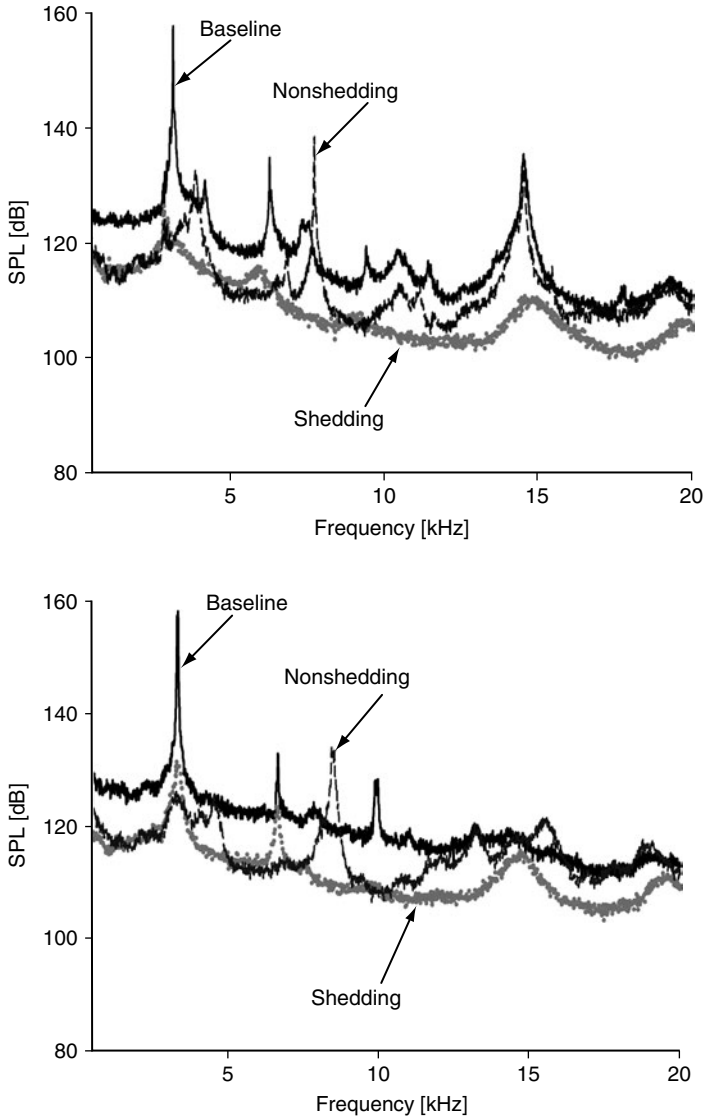

Figure 5. Spectra comparing the acoustic suppression characteristics of shedding and non-shedding configurations. (a). $M = 0.60$, and (b). $M = 0.70$.

axisymmetric mode instabilities can exist for the entire range of stand-off distances where impingement tones are possible.

Figure 7 shows the dispersion relations of the helical instability of the first radial subsonic acoustic mode at $M_j = 0.90$. This figure shows a comparison of the dispersion relation calculated using the vortex-sheet model as well as using the mixing-length model with various momentum thicknesses. It is seen that the dispersion relation calculated using the mixing-length model lies below the permissible Strouhal number limit for small values of the momentum thickness, θ. Even at moderately large θ values, there still exist (ω, α) pairs that lie below the permissible Strouhal number limit. However, at large enough θ values, the dispersion relation lies completely above the permissible Strouhal number limit. Thus, figure 7 shows that the helical modes are permissible for low to moderate θ values; at higher θ values the Strouhal number of the subsonic neutral acoustic modes increases above that permissible for stable impingement tone generation. Restated in terms of the stand-off distance, it follows that if the stand-off distance is such that it lies within the range where the momentum thickness of the jet allows for dispersion relations of the helical mode to lie within permissible Strouhal number limits, one can expect a helical mode to exist. As seen in figure 7, this occurs only for a specific range of θ values, or, in other words, for a specific distance away from the nozzle exit. This means that at $M_j = 0.90$, the helical mode will exist only at small stand-off distances. This is in agreement with our experimental results shown in figures 4(a) and (b).

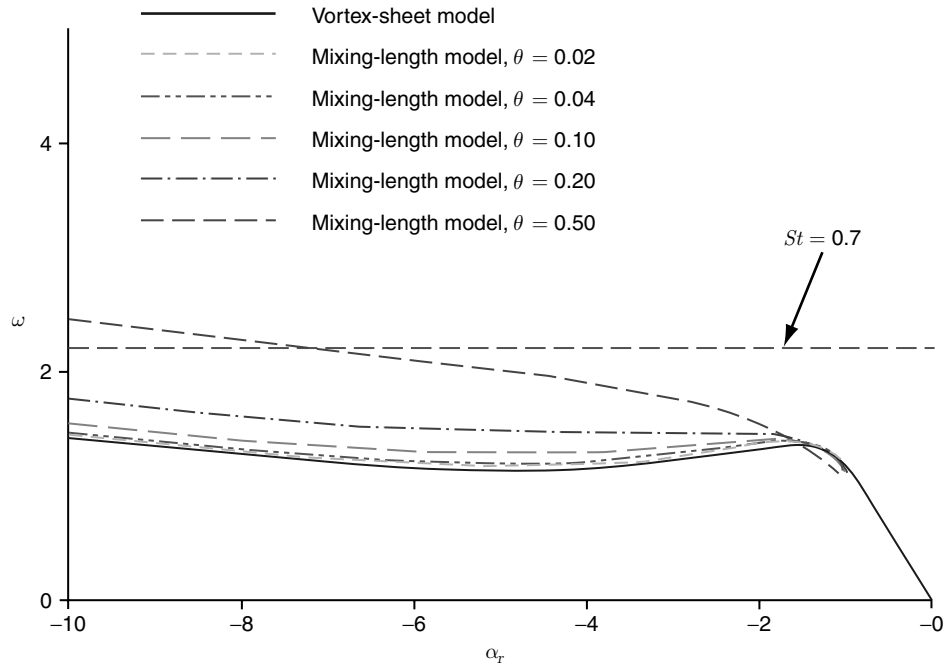

Figure 6. Dispersion relations of the axisymmetric instabilities of the subsonic neutral acoustic mode calculated using the vortex-sheet model and the mixing-length model with various values of the momentum thickness. Cold jet, $M_j = 0.90$, $n = 0$.

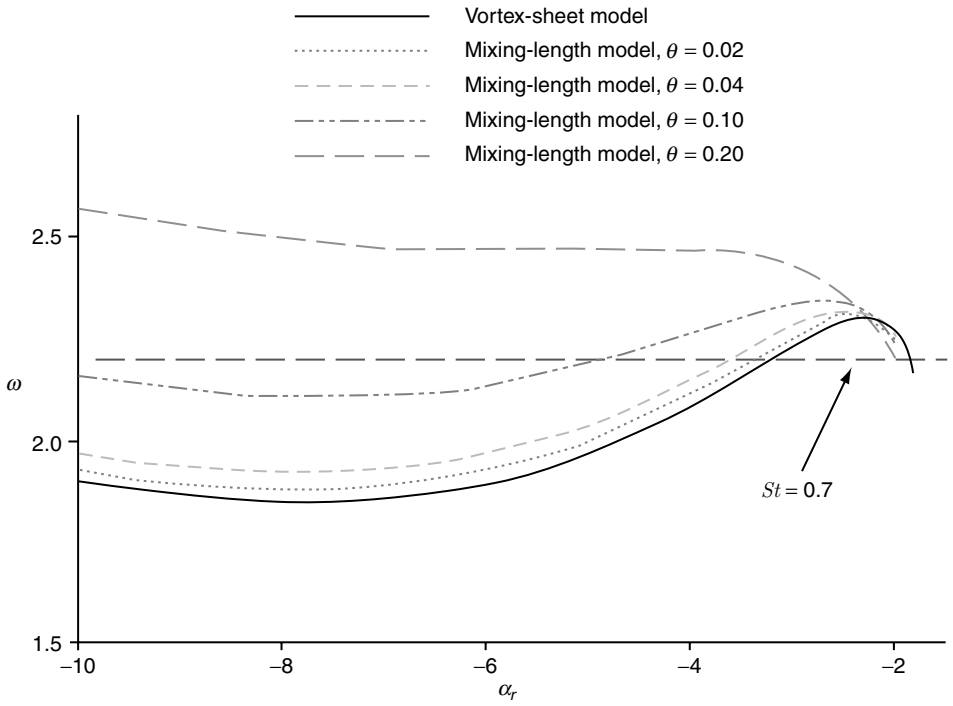

Figure 7. Dispersion relations of the helical instabilities of the subsonic neutral acoustic mode calculated using the vortex-sheet model and the mixing-length model with various values of the momentum thickness. Cold jet, $M_j = 0.90$, $n = 1$.

Figure 8 compares the dispersion relations of the helical instability of the subsonic neutral acoustic mode calculated using the vortex-sheet model and the mixing length model at $M_j = 0.95$. As seen from this figure, for the same momentum thickness values, all the dispersion relation curves lie within the permissible Strouhal number limit. This leads us to conclude that at $M_j = 0.95$, the helical instability mode can persist for a greater distance downstream as compared to $M_j = 0.90$. Once again, this is in agreement with our experimental results shown in figures 4(a) and (b).

Next, we take a look at how the pressure eigenfunction distribution of the helical mode changes when calculated using the vortex-sheet model and the mixing-length model. This comparison is shown in figure 9. The pressure eigenfunction distributions shown in this figure have been normalized by the maximum pressure amplitude in order to facilitate comparison between different cases. This figure shows that for the lower momentum thicknesses, the eigenfunction distributions calculated using the vortex-sheet model and the mixing-length model match closely. For the higher momentum thicknesses,

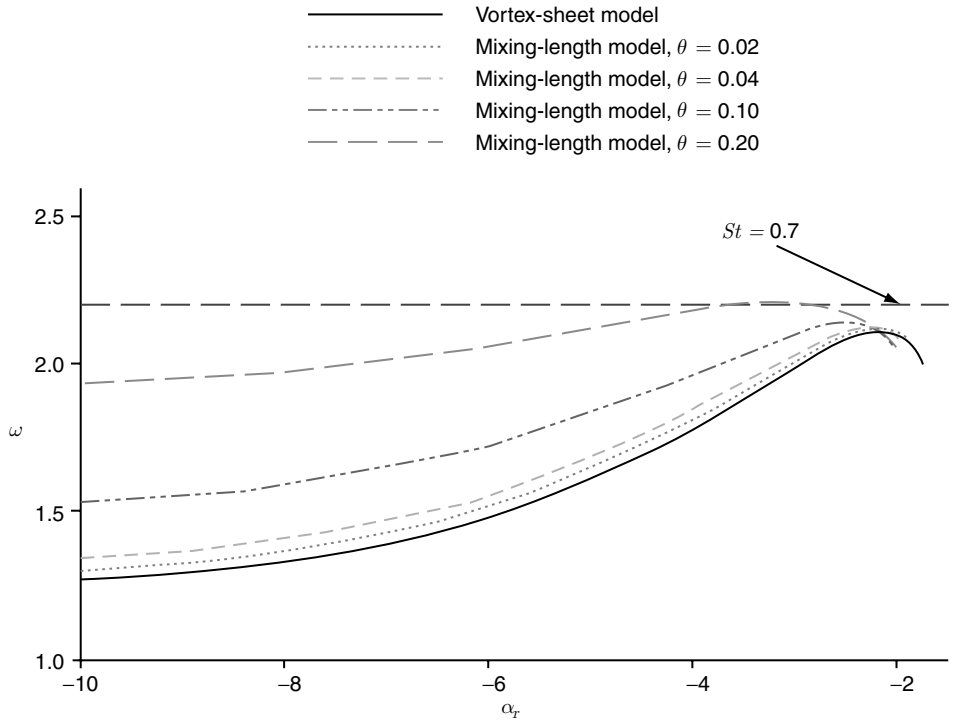

Figure 8. Dispersion relations of the helical instabilities of the subsonic neutral acoustic mode calculated using the vortex-sheet model and the mixing-length model with various values of the momentum thickness. Cold jet, $M_j = 0.95$, $n = 1$.

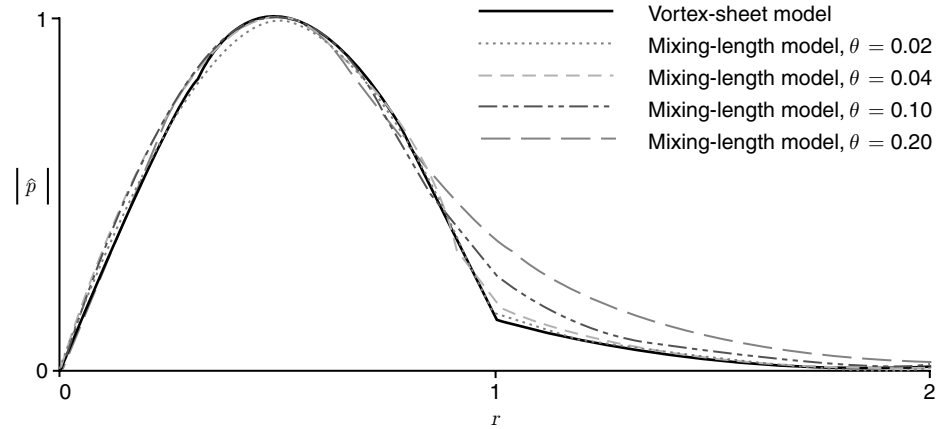

Figure 9. Eigenfunction distribution of the (1,1) mode calculated using the vortex-sheet model and the mixing-length model. Cold jet, $M_j = 0.90$.

the eigenfunction distributions of the mixing-length model match the vortex-sheet model within the jet boundary. However, outside the jet boundary, the mixing-length model shows a greater pressure amplitude compared to the vortex-sheet model. Nevertheless, the dominant pressure fluctuations are confined to within the jet boundary which supports the theory proposed in [18] that the feedback loop in subsonic impinging jets is closed from within the jet column.

We now focus on the issue of predicting a stand-off distance where we can expect helical modes to contribute to the acoustic feedback mechanism. In the experimental data of Panickar and Raman[19], it was seen that the helical modes existed (or were dominant) only when the stand-off distances were small. This was explained by the fact that the Kelvin-Helmholtz instabilities that had smaller wavelengths (or higher frequencies) were spatially decayed at a very rapid rate, and the only way they could contribute to the resonance mechanism was if the stand-off distance was small. Using the least-dispersive wave theory for the neutral acoustic modes, it was shown that the helical mode instabilities occur at frequencies that are greater than those at which axisymmetric instabilities occur which meant that they could only be dominant when the stand-off distances are small. Since the experimental instability frequency agreed very closely with the frequency of the least dispersive wave, one could use this theory to predict the instability frequency of an impinging jet. If this theory is applied to the mixing length model, one can calculate the least dispersive wave of an impinging jet operating at a given Mach number for a range of values of the momentum thickness. By doing so, one arrives at a value of the momentum thickness where the Strouhal number at the given Mach number exceeds the permissible limit of $St = 0.7$. Then, using a correlation between momentum thickness and axial distance similar to the one shown in equation (29), one can estimate the the range of stand-off distances where the helical mode can exist and contribute to the acoustic feedback mechanism.

Figure 10 shows the variation in the Strouhal number of the least dispersive wave at three different jet Mach numbers for a range of momentum thicknesses. The Strouhal number corresponding to $\theta = 0$ is the value obtained using the vortex-sheet model. As seen from this figure, at $M_j = 0.95$, the least dispersive wave lies within the permissible range of Strouhal numbers for a large range of θ values. On the other hand, at $M_j = 0.90$, there is a relatively small range of θ values that lie within the permissible range; at $M_j = 0.85$ the jet column cannot sustain the helical instability for any value of θ. This indicates that at $M_j = 0.95$, the jet column can sustain the helical instability mode for a comparatively larger range of stand-off distances than at $M_j = 0.90$. This was experimentally verified, and the spectra shown in figures 11(a) and (b) show the instabilities present at $M_j = 0.90$ and 0.95, respectively, at a stand-off distance of $h/D_j = 3.0$. As seen from this figure, the time averaged spectrum at $M_j = 0.95$ still shows the presence of a helical instability which is not seen at $M_j = 0.90$.

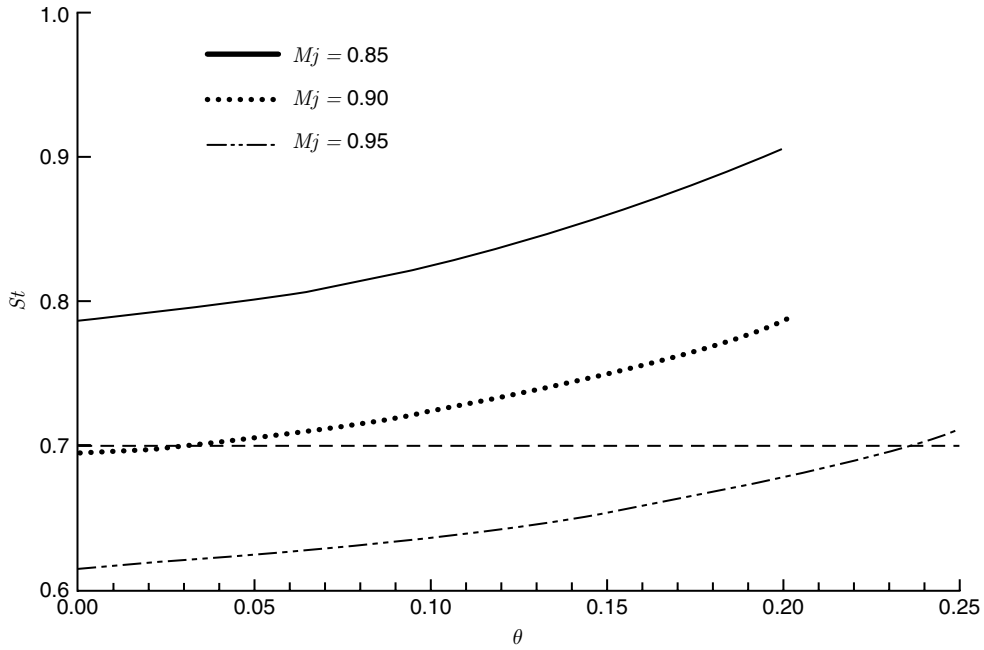

Figure 10. Least dispersive wave of the helical ($n = 1$) instability mode for a cold jet.

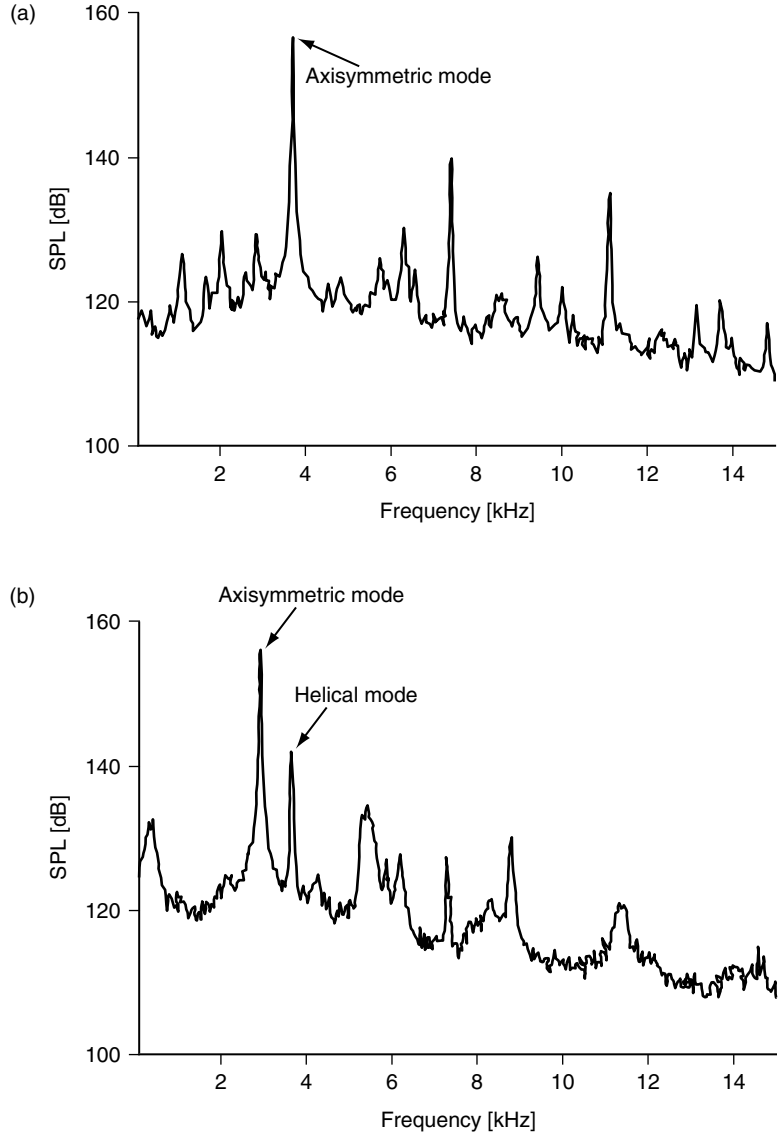

Figure 11. Spectra for impinging jet at (a). $M_j = 0.90$, and (b). $M_j = 0.95$ showing the existence of helical mode at $M_j = 0.95$ but not at $M_j = 0.90$. $h/D_j = 3.0$.

On the basis of the data presented in figure 10, one can arrive at a relation for the momentum thickness, θ, as a function of the jet Mach number, M_j, where $St = 0.7$ for the least dispersive wave. This graph is shown in figure 12. As the jet Mach number increases, the momentum thickness where the Strouhal number limit is reached, increases. This confirms that the helical instability can be sustained for a larger stand-off distance before the Strouhal number mismatch causes acoustic resonance in the helical mode to cease. This is in complete agreement with our experimental data.

6.2. Cavity Flows and the Two-Dimensional Rayleigh Equation

6.2.1. Streamwise Evolution of Mean Velocity Profiles

Detailed measurements of the mean velocity profiles along the centerline of the cavity will help us understand the differences in the development of the shear layer for various configurations. Additionally, the experimentally measured mean velocity profile near the upstream edge of the cavity were used to perform stability calculations that helped determine the most unstable frequencies for a given configuration.

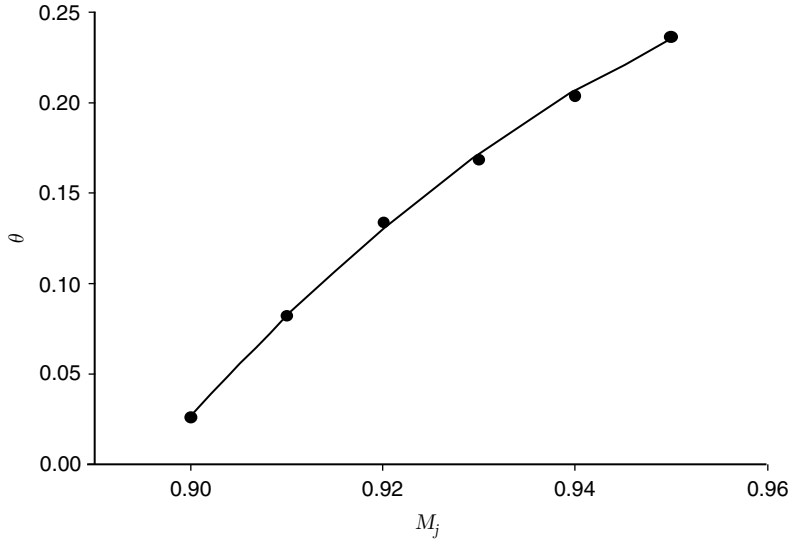

Figure 12. Momentum thickness of the least dispersive helical instability mode for a cold jet.

The mean velocity profiles for the baseline and two control configurations are shown in figure 13. The symbols are the experimentally measured values and the solid curve through the symbols is the best fitting curve through these measurements using equations (31) or (32), as applicable. Figure 13(a) shows that, for the baseline configuration, the agreement between the theoretical curves and experimental data is good for the upstream location although it gets progressively worse as the shear layer spreads out in the transverse direction. The spreading of the shear layer becomes evident at streamwise locations downstream of $x = 0.4$ where the mean profiles indicate that the total pressure probe detects velocities at transverse locations $y < 0$, i.e. inside the cavity. It must, however, be pointed out that even at the downstream locations, the agreement of the experimental data with equation (31) is good in regions above the cavity and the disconnects between the measured and theoretically expected profiles are only present within the cavity. This is similar to the data presented in Rowley, Colonius and Basu[40] where it was found that the recirculating region towards the downstream end of the cavity leads to flow reversal within the cavity and progressive worsening of the agreement with the theoretical curve in this region, although the agreement is good in the regions outside the cavity. This strong recirculating zone in the downstream region of the cavity is indicative of strong interaction between the shear layer and the downstream edge of the cavity, which is necessary for setting up and maintaining strong resonant tones.

For the nonshedding configuration (figure 13(b)), the experimental datapoints once again agree well with a curvefit following equation (31). Additionally, there was no velocity detected within the cavity at any streamwise location by the total pressure probe. These two observations make it clear that, (i). the shear layer for the nonshedding configuration develops and spreads in a manner similar to the baseline configuration, and (ii). this shear layer is deflected upwards to such an extent that even though it may spread, this spreading is not enough for the flow to penetrate into the cavity. This lack of flow within the cavity can be seen for the experimental datapoints and the best fitting curve, both of which indicate zero velocity below $y < 0$. For this nonshedding configuration, the agreement between experimental data and theoretical curves is found to be good at all streamwise locations unlike the baseline configuration. This would indicate the absence of the recirculating zone and the associated flow reversal that exists in the baseline configuration. This indicates that in the nonshedding configuration, the interaction between shear layer and the downstream end of the cavity is attenuated.

The velocity deficit in the wake of the cylinder is clearly visible at all the streamwise locations for the shedding configuration (figure 13(c)). At $y \sim 0.0$ a top-hat type of wake profile is seen for regions just downstream of the cylinder where the total pressure probe detects zero velocity. Further downstream, the wake is diffused and simultaneously deflected away from the cavity. Moreover, the probe detects mean velocity in the regions where $y < 0$, although not as deep within the cavity, as seen for the baseline configuration. In fact, for the shedding configuration, it is seen that the shear layer spreads such that the flow initially penetrates into the cavity at locations immediately downstream of the rod.

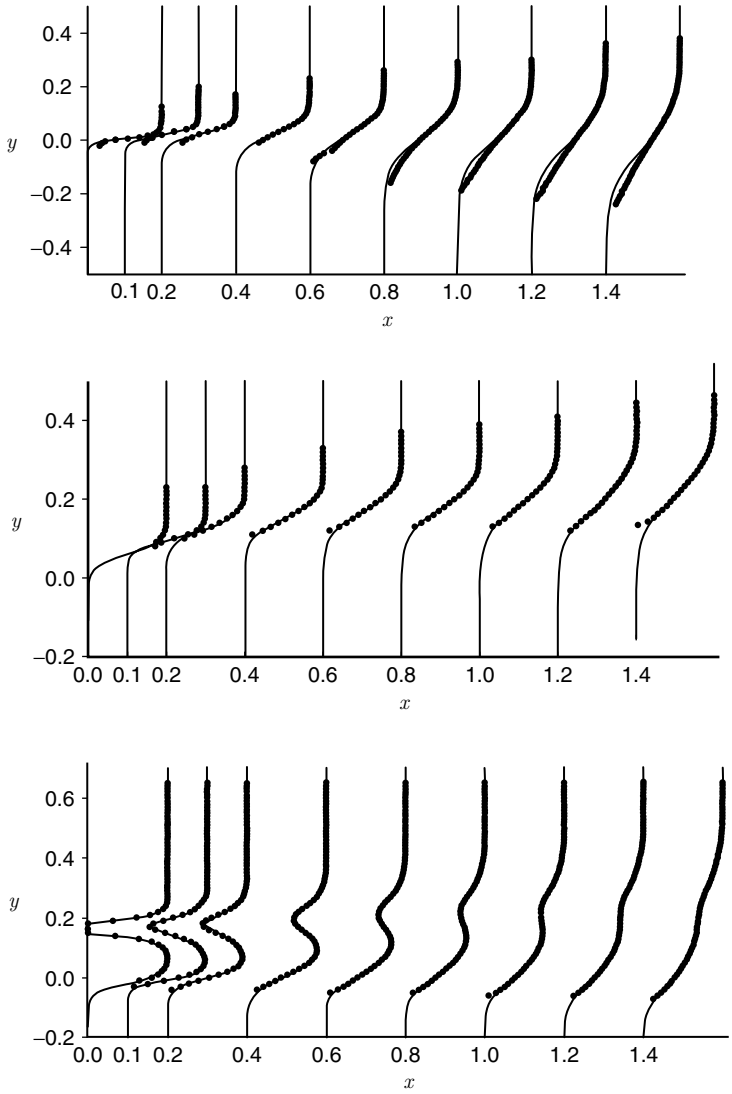

Figure 13. Distribution the mean velocity profile for the (a). Baseline, (b). Nonshedding, and (c). Shedding configurations at M = 0.60 at various streamwise locations.

Since the experimentally obtained mean velocity data for the baseline and nonshedding configurations can be curvefitted using a similar hyperbolic tangent type relation given in equation (31), the rationale regarding why the former configuration shows strong resonance characteristics and the latter shows diminished resonance characteristics must lie in the parameters of this equation. The curvefits of the experimental data for the baseline and nonshedding configurations give us an estimate of the vorticity thickness at each streamwise location and, for a number of such locations, helps in the calculation of the spreading rate of the shear layer. Additionally for these two configurations, the deflection of the shear layer at progressive streamwise locations can also be compared. Figure 14 shows the streamwise spreading rate of the shear layer for the baseline and nonshedding configurations as determined by the variation in the vorticity thickness along the streamwise direction. As shown in this figure, the growth rates for both configurations are reasonably linear as shown by the best fitting linear curve to the experimentally measured datapoints indicated by the symbols. It should be noted that the length scale is nondimensionalized by the vorticity thickness at the most upstream location, similar to the method followed in [40], which means that both the calculated datapoints and the best fitted curve have a y-intercept equal to 1. The growth rate for each configuration is estimated as the slope of this best-fitting line. As the numbers on the graph indicate, the growth rate for the nonshedding configuration is found to be 58% less than the growth rate of the baseline configuration. Although the theoretically accepted growth rate for turbulent mixing layers is around 0.162, values as high as 0.181 have also been measured in the experiments by Brown and Roshko[41]. Thus, for the baseline configuration it is

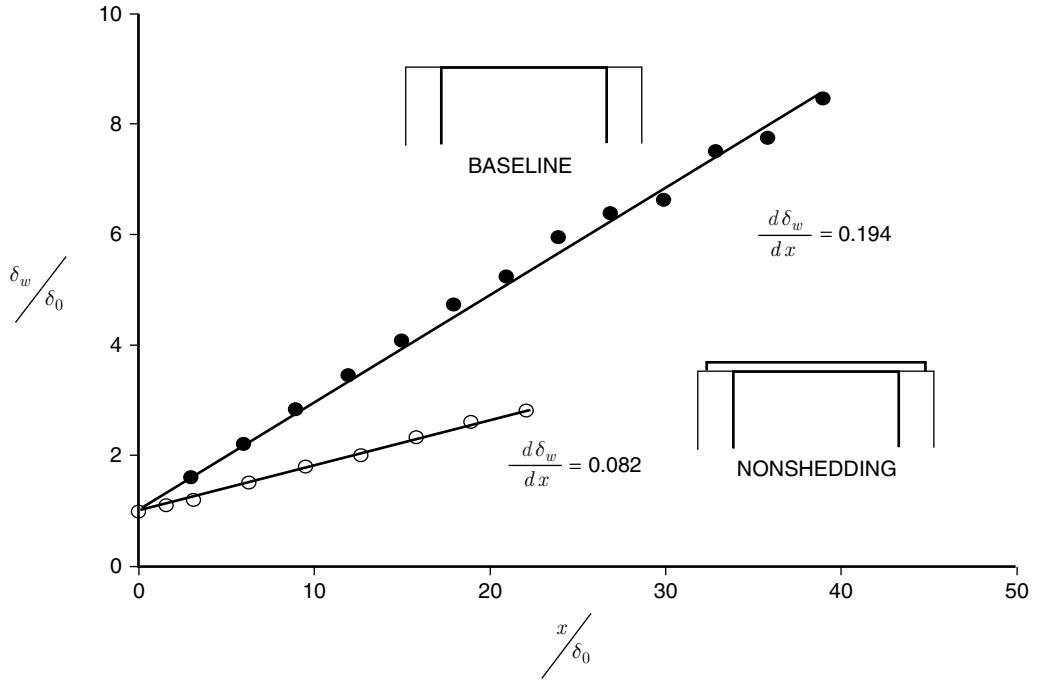

Figure 14. Shear layer spreading rates for the baseline and nonshedding configurations. Also shown is the best fitting linear curve to the experimental data and the slope of this line. $M = 0.60$.

reasonable to conclude that the shear layer spreading rate of 0.194 is indicative of a turbulent free shear layer.

For laminar shear layers, as reported in [40], the results of Sarohia[42] indicate that as L/θ_0 was increased from 52.5 to 105.2, the spreading rate varied between $d\delta_w/dx = 0.025$ to 0.088. That is to say, for a lower value of L/θ_0, the shear layer would have a smaller growth rate as compared to a turbulent shear layer. This is in agreement with results for our nonshedding configuration that had a shear layer growth rate of $d\delta_w/dx = 0.082$. Thus, the shear layer spreading rate measurements indicate that the nonshedding configuration spreads in accordance with a laminar free shear layer. This information will be relevant when comparing experimental results to predictions from linear stability theory.

The shear layer deflection for the baseline, nonshedding and shedding configurations is shown in figure 15. Note that, given the form of equations (31) and (32), a negative value of SL_{off} is representative of the flow being deflected away from the cavity, whereas a positive value of SL_{off} is representative of the flow being deflected into the cvity. The dramatic lift-off of the shear layer due to the presence of the rod on the upstream edge of the cavity in the nonshedding configuration is clearly seen from this graph. In comparison, the deflection produced by the shear layer for the baseline configuration is extremely small at the upstream locations. As one moves further downstream, the shear layer is observed to be deflected into the cavity. The shedding configuration does result in a lift-off of the shear layer. However, this occurs downstream of $x = 0.3$ and its magnitude is much smaller than the lift-off produced by the nonshedding configuration. In fact, it is seen that upstream of $x = 0.3$, the cylindrical rod sheds vortices that cause the flow to initially deflect *into* the cavity.

Thus, for the nonshedding configuration, the spectra (which shows the dominance of a Rossiter mode different from that in the baseline) and shear layer offset data taken together indicate that the nonshedding configuration behaves similar to a shear layer lift-off device and acts as a detuning mechanism for the resonant feedback loop. The drawbacks of using such a control method lie in the fact that it cannot be relied on to give consistent performance at all flow conditions since the magnitude of the shear layer lofting will depend on the freestream Mach number.

The acoustic results from our study are in broad agreement with the results presented in Ukeiley *et al.*[30]. This latter study was more detailed in the sense that it looked at the effect of changing various geometric parameters on the cavity resonance suppression mechanism using a fence and a cylindrical rod-in-crossflow arrangement. The measured mean velocity profiles in the current study

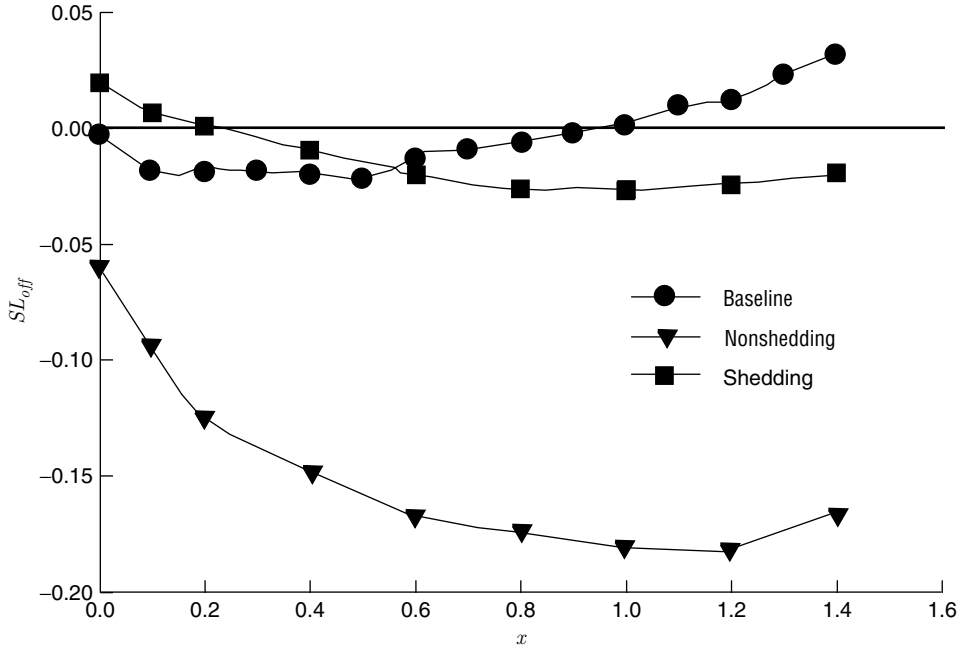

Figure 15. Deflection of the shear layer in the streamwise direction lor the basline and two control configurations, M = 0.60.

show very good qualitative agreement with the measured profiles in [30] (see, for instance, figure 7 in their paper). The mean velocity profiles for their configuration with the fence clearly show the lifting of the shear layer as a result of the solid fence. Additionally, their study shows the importance of correctly choosing the gap between the shedding cylinder and the upstream edge. For too small a gap, the velocity profile, in spite of showing an inflection, was significantly deflected upwards such that the first location where velocity was detected lay above the cavity. Increasing this gap moved the mean profile downwards, but the first location where velocity was detected was still close to a wall normal distance of 0. However, keeping the gap constant and decreasing the diameter of the cylinder, i.e. allowing more room for the development of the wake, finally moved the first measured location to lie within the cavity.

Thus, from our study of the streamwise evolution of the mean velocity for the baseline and control configurations it becomes clear that the shedding configuration does not provide shear layer lift-off to the same extent as that of the nonshedding configuration. Thus, the fact that the shedding configuration provides more acoustic suppression than the nonshedding configuration points to an alternate mechanism governing its dramatic resonance suppression characteristics.

6.2.2. Spatial Linear Stability Analysis of Experimental Mean Velocity Profiles

We now calculate the spatial growth rate of the experimentally measured mean velocity profiles for the baseline and two control configurations. The curve plotting the growth rate as a function of the instability frequency gives us an envelope of the most amplified frequencies corresponding to the particular mean velocity profile. The mean velocity profiles used for the stability calculations are the best-fit equations to experimental data, i.e. equations of the form given by equation (31) for the baseline and nonshedding configurations and (32) for the shedding configuration.

The stability calculations were performed for the mean velocity profiles for each configuration at $x = 0.1$. This location is close enough to the upstream edge of the cavity (5% of the cavity length) that the stability calculations for the profiles here provide information regarding the most unstable frequencies in the shear layer for the respective mean velocity profiles. Figure 16 shows the amplification envelope for all the configurations. Note that the frequencies on the *X*-axis of the stability curves are presented as Strouhal numbers using the appropriate length scales. As shown in the figure, the Strouhal numbers are related to the nondimensional frequencies by a scaling factor of 2π. Note that for the hybrid velocity profile, there exist two separate instability modes. These instability modes are dependent on the wake part and the shear layer part of the velocity profile and are designated as mode

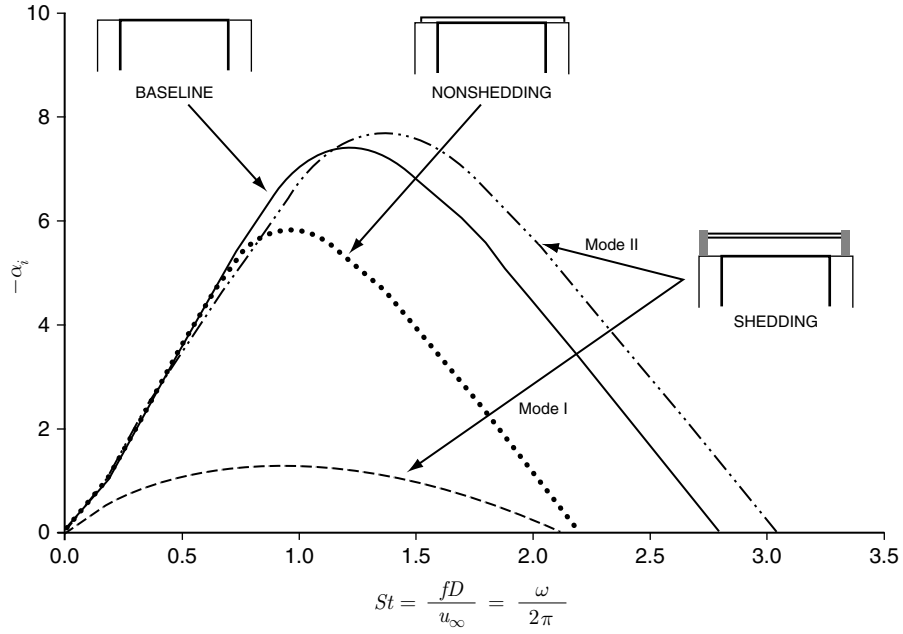

Figure 16. Envelope of most amplified frequencies from linear stability theory for the baseline and two control configurations for the experimental velocity profiles at $x = 0.1$; $M = 0.60$.

I and mode II respectively. The work of Koochesfahani and Frieler[39] referred to these modes as the wake mode and the shear layer mode respectively. The characteristics of these modes and their variation with the parameters of the hybrid profile are discussed in greater detail in Sarpotdar, Panickar and Raman[43]. Figure 16 shows that the growth rate of instability mode I of the shedding configuration (the so called 'wake mode' as per [39]) is much smaller than that of the baseline, nonshedding or mode II of the shedding configurations. The growth rates of the baseline, nonshedding and shedding-mode II configurations are all dependent on the measured (and curvefitted) value of the vorticity thickness, δ_w, at $x = 0.1$. A larger value of δ_w results in a smaller maximum growth rate and smaller range of instability frequencies.

Next, we present results from experimental measurements of instability growth rates and compare these measurements to predictions from linear stability theory. For the baseline and nonshedding configurations, the magnitude of the instability wave at the resonant frequency ($\mathrm{R1}$ for the baseline and $\mathrm{R2}$ for the nonshedding configuration) is calculated based on the shear layer spreading rate information shown in figure 14. At each streamwise location, based on the vorticity thickness estimated from the shear layer spreading rate, the value of the wavenumber, α, was used to obtain the amplitude of the instability. Since α is a slowly varying function of the streamwise coordinate x, the resulting magnitude is not strictly linear (when plotted on a logarithmic scale), but provides us with a much better estimate of the amplitude of the instability. The experimental data corresponds to the maximum amplitude of the fluctuating pressure signal of the instability mode of interest in the shear layer at a given streamwise location. For the experimental data, the amplitude has been suitably scaled in order to facilitate comparison with results from the stability calculations.

We begin by examining data for the baseline configuration. Figure 17(a) shows a comparison of the instability wave magnitude for the first Rossiter mode ($\mathrm{R1}$) between experimental data and linear stability theory. The shear layer spreading rate for the baseline configuration is close to that of a turbulent free shear layer as was shown in figure 14. Figure 17(a) shows that the experimentally calculated amplitudes of the $\mathrm{R1}$ instability mode initially decrease before increasing in the streamwise direction. There is good agreement between experiment and theory in the streamwise regime where the experimental results indicated that instability wave magnitude is amplified. Figure 17(b) shows power spectral density (PSD) plots at various streamwise locations measured using a Kulite probe traversing the shear layer. These measurements were taken along the spanwise centerline of the cavity, i.e. along $z = 0$. The PSD plot for each successive streamwise location is shifted up by two decades in order to view these spectra more clearly. At each streamwise location, the first Rossiter mode frequency at

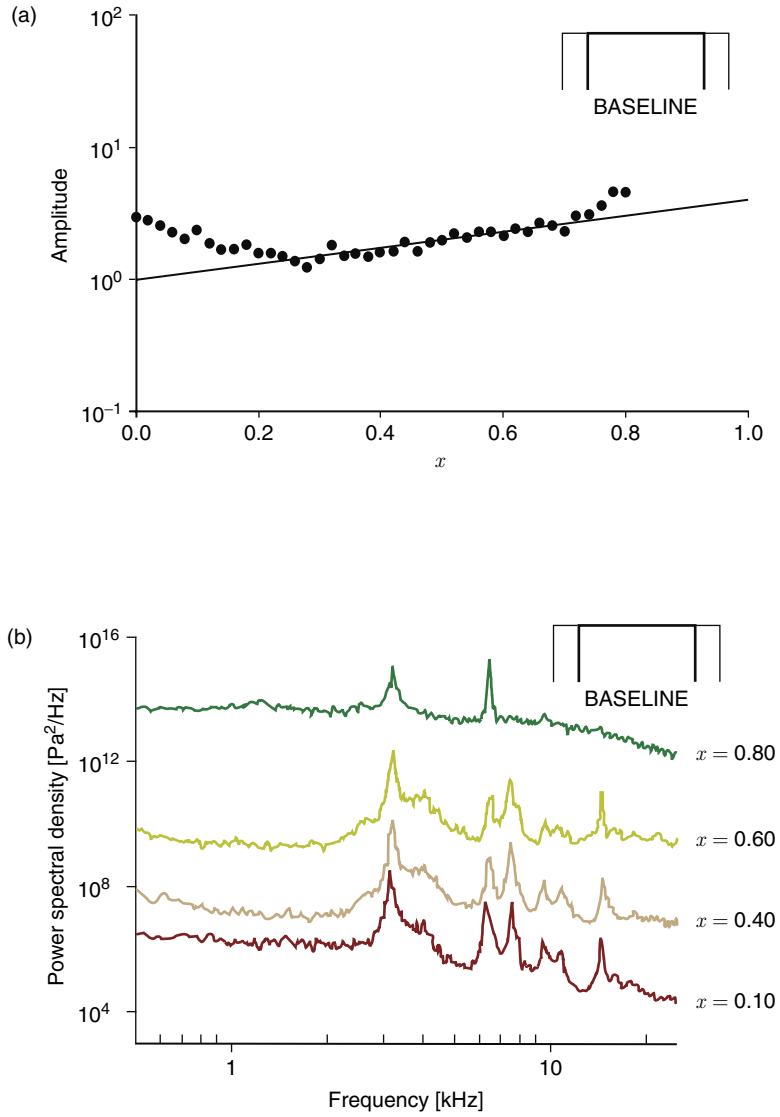

Figure 17. Instability mode characteristics of the baseline configuration, $M = 0.60$.
(a). Comparison of the instability amplitude of the first Rossiter mode, (R1), calculated from experimental data and linear stability theory. Symbols represent experimental data, solid curve represents results from stability analysis. (b). Streamwise variation of the hydrodynamic instabilities in the shear layer showing the persistence of the R1 instability mode. Note that the PSD spectra for successive downstream locations have been shifted up by two decades from the preceding one for the sake of clarity.

3200 Hz can be clearly discerned and this frequency persists at all streamwise locations, albeit at different amplitudes. This is to be expected since it is this instability that interacts with the downstream edge of the cavity and gives rise to strong acoustic tones.

For the nonshedding configuration, the comparison of the instability magnitude between experiment and theory for the second Rossiter mode, R2, is shown in figure 18(a). Keeping in mind that the shear layer spreading rate for this configuration is similar to that of a laminar free shear layer, it can be seen that there is excellent agreement between theory and experiments beginning at the upstream edge of the cavity up to a streamwise distance of $x \sim 0.5$. The streamwise variation of the PSD for the nonshedding configuration is shown in figure 18(b). The persistence and growth of the the second Rossiter mode at 7500 Hz in the streamwise direction can be clearly discerned from the spectral plots and is in agreement with the growth rates predicted by linear stability calculations. These plots lend greater credibility to

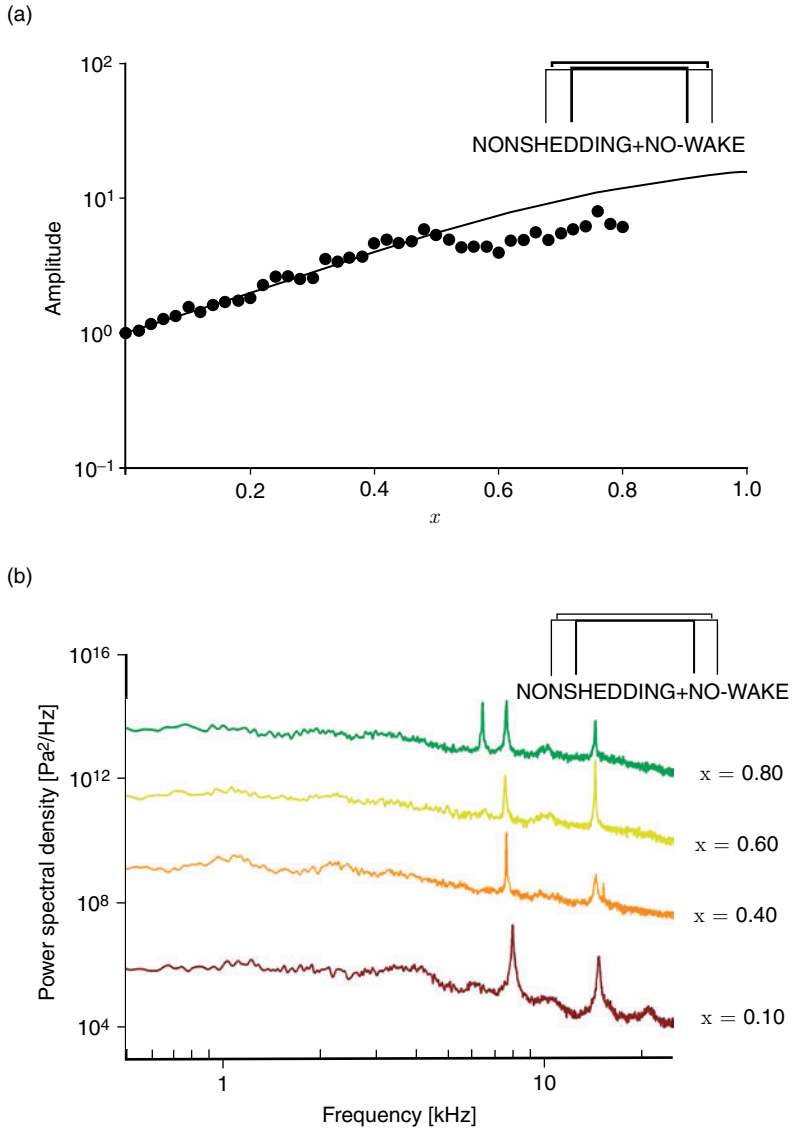

Figure 18. Instability mode characteristics of the nonshedding configuration, $M = 0.60$.
(a). Comparison of the instability amplitude of the second Rossiter mode, R2, calculated from experimental data and linear stability theory. Symbols represent experimental data, solid curve represents results from stability analysis, (b). Streamwise variation of the hydrodynamic instabilities in the shear layer showing the persistence of the R2 mode. Note that the PSD spectra for successive downstream locations have been shifted up by two decades from the preceding one for the sake of clarity.

the proposition that the acoustic suppression afforded by the nonshedding configuration is a result of detuning the acoustic feedback loop from the R1 mode, since, as figure 18 shows, the amplification mechanism in the shear layer remains intact, albeit for the R2 mode.

For the shedding configuration, the experimental data revealed no spatially amplifying instability. Figure 19 shows the PSD plots at a variety of streamwise locations for the vortex shedding configuration. Once again, the plot for each successive downstream location is shifted upwards by two decades to facilitate better viewing of the graphs. As seen from these plots, the amplitude of shedding frequency reduces rapidly for progressive streamwise locations and at $x = 0.80$ and all subsequent downstream locations, the spectra in the shear layer becomes featureless and no longer indicates the presence of any dominant structures.

Finally, since the shedding configuration has proven to be the most effective at suppressing the resonant acoustic component present in the baseline flow, we examine the nature of the shedding from the cylinder

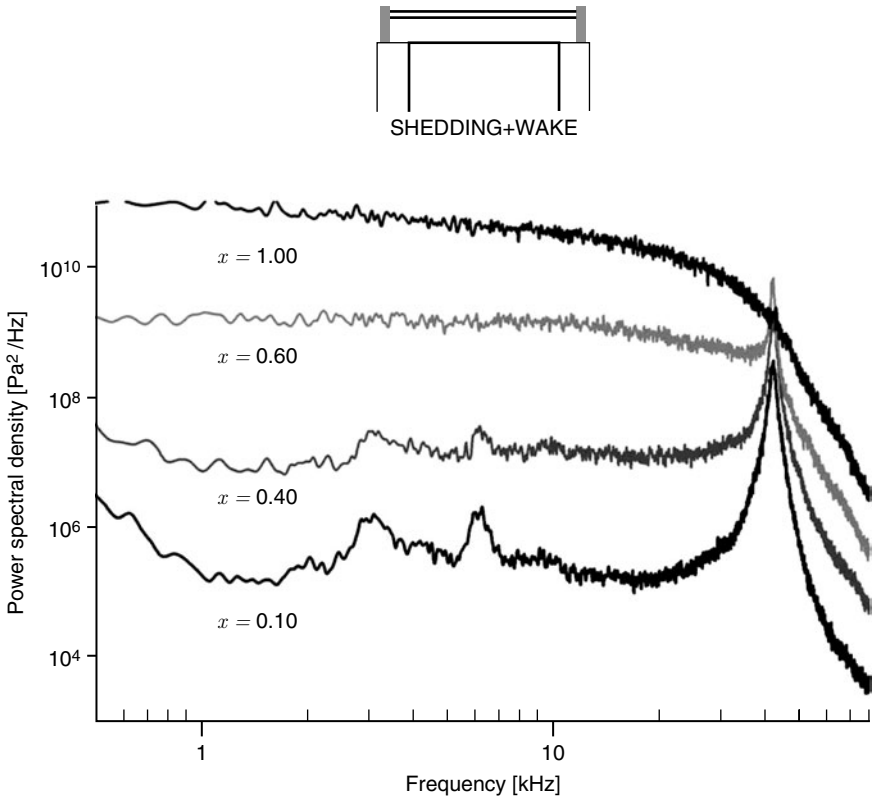

Figure 19. Streamwise variation of the hydrodynamic instabilities in the shear layer for the shedding configuration showing the gradual decay of the shedding instability, $M = 0.60$. Note that the PSD spectra for successive downstream locations have been shifted up by two decades from the preceding one for the sake of clarity.

with regards to its spanwise structure. Figure 20 shows the streamwise evolution of the spanwise coherence at the shedding frequency. The spanwise coherence was quantified by measuring the phase difference between a reference signal (the microphone located at the cavity floor) and a Kulite traversing in the wake of the cylinder at the shedding frequency. For a given streamwise location, the Kulite was located at $y = 0.165$ and traversed in the spanwise direction from $z = -1$ to $z = 1$. These measurements were repeated at a number of streamwise locations until it was found that the spanwise shedding had become incoherent. As figure 20 shows, the shedding is spanwise coherent near the upstream edge of the cavity. As we move in the streamwise direction, the shedding starts becoming incoherent in the regions near the sidewalls of the cavity. This region of incoherence starts spreading inwards towards the spanwise centerline of the cavity for locations that are further downstream. At locations downstream of $x = 0.6$, no spanwise coherence could be detected at the shedding frequency. This is in agreement with the PSD data in the shear layer for the vortex shedding configuration shown in figure 19 which shows that the amplitude of the instability at the shedding frequency reduces in the streamwise direction. The data shown in figure 20 leads us to conclude that this decay in instability amplitude at the shedding frequency is accompanied by a decline in spanwise coherent vortex shedding. This is an important consideration that must be taken into account when designing the resonance control device. Linear stability analysis tells us that any frequency that lies outside the amplification envelope can, potentially, be used to provide the high frequency excitation since the instabilities at all these frequencies will decay spatially. However, an effective high frequency excitation device will be one that introduces the excitation at high-enough frequencies that typically have spatial *decay rates* that are much greater than the stable modes at lower frequencies.

7. CONCLUDING REMARKS

In this paper, we used elements from linear stability analysis and the compressible Rayleigh equation in order to gain insight into the physical mechanisms of two separate resonant acoustic flows. In the case of impinging jets it was seen that the instability mode that is responsible for the acoustic feedback is related to the stand-off distance via the momentum thickness parameter. In this study we focused our

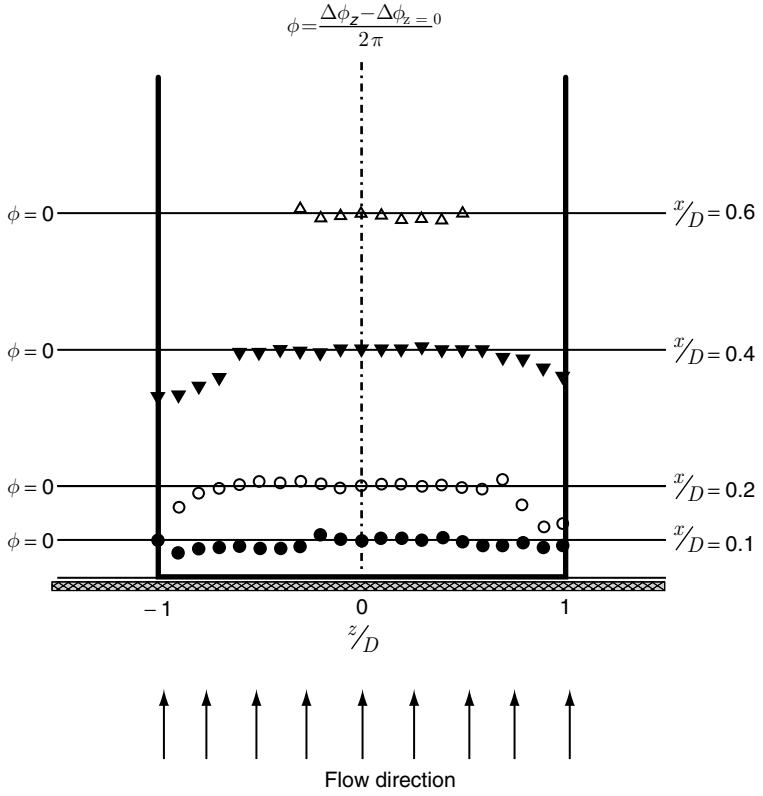

Figure 20. Streamwise evolution of the phase angle. The phase angle at a given streamwise location is calculated as the difference between the local phase angle and the phase angle at $z = 0$ at the same streamwise location. The horizontal line at each streamwise location corresponds to a phase angle, $\theta = 0$. As seen, the shedding is spanwise coherent except near the side walls of the cavity. For progressively downstream streamwise locations, this coherence breaks up and finally, downstream of $x = 0.60$ no spanwise coherent structures are discernible.

interest on the helical instability mode since it is this mode that can lead to jet interactions when nozzles are operated in twin configuration. As the momentum thickness is increased, the dispersion relation of the subsonic helical acoustic mode changes such that its Strouhal number lies outside the permissible range ($St \leq 0.7$), as per theory. A systematic study revealed that at high subsonic Mach numbers, the Strouhal number of the least dispersive wave at a given value of the momentum thickness (θ) lies within the permissible range for a wider range of θ values. Since the momentum thickness of a developing jet can be directly related to the streamwise location in the flow, this meant that, knowing the spreading rate of the jet, one could calculate a range of stand-off distances where helical modes could exist.

As far as cavity resonance flows are concerned, this paper demonstrated the effects of two resonance control mechanism on the physical evolution of the flow along the centerline of the cavity. Although both control configurations lifted the shear layer off to some extent, only the nonshedding configuration did it to an extent that de-tuned the feedback loop present in the baseline configuration. The shedding configuration led to an initial deflection of the shear layer into the cavity before lofting it to a much smaller extent than the nonshedding configuration. Linear stability analysis of the experimentally measured mean velocity profiles revealed that of the two instability modes present in the shedding configuration, mode I had growth rates much smaller than the baseline. On the other hand, the growth rates of mode II were comparable to those in the baseline. Experimental data acquired to verify the stability results showed good agreement.

It is hoped that the results presented in this paper will offer better insight into designing effective resonance control devices for both, impinging jets as well as cavity flows, for future aerospace applications.

ACKNOWLEDGEMENTS

The authors are grateful to Dr. Alan Cain of ITAC, LLC and Dr. Michael Stanek of the AFRL for their insightful comments and suggestions and to Dr. Clarence Rowley of Princeton University who provided guidance with linear stability analysis.

REFERENCES

1. G. Raman, E. J. Rice, and E. Reshotko, Mode spectra of natural disturbances in a circular jet and the effect of acoustic forcing, Experiments in Fluids **17**, 415 (1994).
2. G. Raman and A. B. Cain, Innovative actuators for active flow and noise control, Journal of Aerospace Engineering **216**, 303 (2002).
3. G. Raman and E. J. Rice, Axisymmetric jets forced by fundamental and subharmonic tones, American Institute of Aeronautics and Astronautics Journal **29**, 1114 (1991).
4. G. Raman, Advances in understanding supersonic jet screech: Review and perspective, Progress in Aerospace Sciences **34**, 45 (1998).
5. G. Raman, Supersonic jet screech: Half-century from Powell to the present, Journal of Sound and Vibration **225**, 543 (1999).
6. G. Neuwerth, Acoustic feedback phenomena of the subsonic and hypersonic free jet impinging on a foreign body, NASA TT **F-15719** (1974).
7. A. Roshko, Some measurements of flow in a rectangular cutout, Technical report, California Institute of Technology, Pasadena, CA, 1955.
8. K. Krishnamurty, *Sound radiation from surface cutouts in high speed flow*, PhD thesis, California Institute of Technology, 1956.
9. J. E. Rossiter, Wind tunnel experiments on the flow over rectangular cavities at subsonic and transonic speeds, Technical report, Aeronautical Research Council Reports and Memoranda, No. 3438, London, England, 1966.
10. H. H. Heller, D. G. Holmes, and E. E. Covert, Flow induced pressure oscillations in shallow cavities, Journal of Sound and Vibration **18**, 545 (1970).
11. L. N. Cattafesta, D. R. Williams, C. W. Rowley, and F. Alvi, Review of active control of flow-induced cavity resonance, American Institute of Aeronautics and Astronautics Paper 2003–3567 (2003).
12. C. W. Rowley and D. R. Williams, Dynamics and control of high-Reynolds-number flow over open cavities, Annual Review of Fluid Mechanics **38**, 251 (2006).
13. G. Raman, S. Khanafseh, A. B. Cain, and E. Kerschen, Development of high bandwidth powered resonance tube actuators with feedback control, Journal of Sound and Vibration **269**, 1031 (2004).
14. A. Marsh, Noise measurements around a subsonic air jet impinging on a plane, rigid surface, Journal of the Acoustical Society of America **33**, 1065 (1961).
15. F. R. Wagner, The sound and flow field of an axially symmetric free jet upon impact on a wall, NASA TT **F-13942** (1971).
16. P. J. Morris, The spatial viscous instability of axisymmetric jets, Journal of Fluid Mechanics **77**, 511 (1976).
17. P. J. Morris and T. R. S. Bhat, The spatial stability of compressible elliptic jets, Physics of Fluids **7**, 195 (1995).
18. C. K. W. Tam and K. K. Ahuja, Theoretical model of discrete tone generation by impinging jets, Journal Fluid Mechanics **214**, 67 (1990).
19. P. Panickar and G. Raman, Criteria for the existence of helical instabilities in subsonic impinging jets, Physics of Fluids **19**, 106103.1 (2007).
20. J. M. Seiner, J. C. Manning, and M. K. Ponton, Dynamic pressure loads associated with twin supersonic plume resonance, American Institute of Aeronautics and Astronautics Journal **26**, 954 (1988).
21. Y. V. Vlasov and A. S. Ginevskiy, Generation and suppression of turbulence in an axisymmetric turbulent jet in the presence of an acoustic influence, NASA-TT **F-15721** (1974).
22. J. M. Wiltse and A. Glezer, Direct excitation of small-scale motions in free shear flows, Physics of Fluids **10**, 2026 (1998).

23. A. B. Cain, M. M. Rogers, V. Kibens, and G. Raman, Simulations of high-frequency excitation of a plane wake, American Institute of Aeronautics and Astronautics Paper 2001–0514 (2001).
24. A. B. Cain, M. M. Rogers, and V. Kibens, Characterization of high-frequency excitation of a wake by simulation, American Institute of Aeronautics and Astronautics Paper 2003–0179 (2003).
25. M. Stanek, G. Raman, V. Kibens, J. Ross, J. Odedra, and J. W. Peto, Control of cavity resonance using very high frequency forcing, American Institute of Aeronautics and Astronautics Paper 2000–1905 (2000).
26. S. F. McGrath and L. L. Shaw, Active control of shallow cavity acoustic resonance, American Institute of Aeronautics and Astronautics Paper 1996–1949 (1996).
27. L. Shaw, Active control for cavity acoustics, American Institute of Aeronautics and Astronautics Paper 1998–2347 (1998).
28. M. Stanek, G. Raman, J. A. Ross, J. Odedra, J. W. Peto, F. Alvi, and V. Kibens, High frequency acoustic suppression – The role of mass flow, the notion of superposition, and the role of inviscid instability - A new model (Part II), American Institute of Aeronautics and Astronautics Paper 2002–2404 (2002).
29. S. Arunajatesan, J. D. Shipman, and N. Sinha, Hybrid RANS-LES simulation of cavity flow fields with control, American Institute of Aeronautics and Astronautics Paper 2002–1130 (2002).
30. L. S. Ukeiley, M. K. Ponton, J. M. Seiner, and B. Jansen, Suppression of pressure loads in cavity flows, American Institute of Aeronautics and Astronautics Journal **42**, 70 (2004).
31. M. Gaster, E. Kit, and I. Wygnanski, Large-scale structures in a forced turbulent mixing layer, Journal of Fluid Mechanics **150**, 23 (1985).
32. L. Lees and E. Reshotko, Stability of the compressible laminar boundary layer, Journal of Fluid Mechanics **12**, 555 (1962).
33. A. Michalke, On the inviscid instability of the hyperbolic tangent velocity profile, Journal of Fluid Mechanics **19**, 543 (1964).
34. A. Michalke, On spatially growing disturbances in an inviscid shear layer, Journal of Fluid Mechanics **23**, 521 (1965).
35. C. W. Rowley, *Modeling, Simulation, and Control of Cavity Flow Oscillations*, PhD thesis, California Institute of Technology, Pasadena, 2002.
36. A. Michalke, Survey on jet instability theory, Progress in Aerospace Sciences **21**, 159 (1984).
37. C. K. W. Tam and F. Q. Hu, On the three families of instability waves of high speed jets, Journal of Fluid Mechanics **201**, 447 (1989).
38. D. G. Crighton and M. Gaster, Stability of slowly diverging jet flow, Journal of Fluid Mechanics **77**, 397 (1976).
39. M. M. Koochesfahani and C. E. Frieler, Instability of nonuniform density free shear layers with a wake profile, American Institute of Aeronautics and Astronautics Journal **27**, 1735 (1989).
40. C. W. Rowley, T. Colonius, and A. J. Basu, On self-sustained oscillations in two-dimensional compressible flow over rectangular cavities, Journal of Fluid Mechanics **415**, 315 (2002).
41. G. L. Brown and A. Roshko, On density effects and large structure in turbulent mixing layers, Journal of Fluid Mechanics **64**, 774 (1974).
42. V. Sarohia, *Experimental and analytical investigation of oscillations in flows over cavities*, PhD thesis, California Institute of Technology, Pasadena, 1975.
43. S. Sarpotdar, P. Panickar, and G. Raman, Cavity tone suppression using a rod in cross flow – Investigation of shear layer stability mechanism, American Institute of Aeronautics and Astronautics Paper 2009–0700 (2009).